DRAFT:
Sensitivity of quantum gate fidelity to laser phase and intensity noise

X. Jiang,[1] J. Scott,[1] M. Friesen,[1] and M. Saffman[1,2]

[1] *Department of Physics, University of Wisconsin-Madison, 1150 University Avenue, Madison, WI 53706*
[2] *ColdQuanta, Inc., Madison, WI 53703*

(Dated: August 5, 2022)

The fidelity of gate operations on neutral atom qubits is often limited by fluctuations of the laser drive. Here, we quantify the sensitivity of quantum gate fidelities to laser phase and intensity noise. We first develop models to identify features observed in self-heterodyne noise spectra, focusing on the effects of white noise and servo bumps. In the weak-noise regime, characteristic of well-stabilized lasers, we show that an analytical theory based on a master equation formalism agrees very well with numerical simulations that incorporate phase noise. We compute quantum gate fidelities for one- and two-photon Rabi oscillations and show that they can be enhanced by an appropriate choice of Rabi frequency. We also analyze the influence of intensity noise with spectral support smaller than the Rabi frequency. Our results provide guidance for analyzing and improving gate fidelities in future qubit experiments.

CONTENTS

I. INTRODUCTION

Logical gate operations on matter qubits rely on coherent driving with electromagnetic fields. For solid state qubits these are generally at microwave frequencies of 1-10 GHz. For atomic qubits microwave as well as optical fields with carrier frequencies of several hundred THz are used for gates. High fidelity gate operations require well controlled fields with very low amplitude and phase noise. In this paper we quantify the influence of control field noise on the fidelity of qubit gate operations. While we mainly focus on the case of optical control with visible or infrared lasers, our results are also applicable to high fidelity control of solid state qubits with microwave frequency fields.

Although the limits imposed on gate fidelity by control field noise are of central importance in the quest for improving performance, the topic has received relatively little attention in the literature. Relaxation of qubits in the presence of noise, with and without a driving field was analyzed in [1–7]. The influence of laser noise on atomic qubit control was analyzed in [8, 9] and very recently in [10].

We develop HERE a detailed theory of the dependence of gate fidelity on the noise spectrum of the driving field. We show that the spectral distribution of noise relative to the Rabi frequency of the qubit drive is an important parameter that determines the extent to which noise impacts gate fidelity. When the noise spectrum is peaked near the Rabi frequency the deleterious effects are most prominent. We proceed in Sec. II with a summary of the theory of the laser lineshape and its' relation to self-heterodyne spectral measurements. In Sec. IV we present a master equation description for the coherence of Rabi oscillations with a noisy drive field. A Schrödinger equation based numerical simulation is given in Sec. V, followed by a quasi-static approximation in Sec. **??**. The results obtained are summarized in Sec. VIII.

II. LASER NOISE ANALYSIS

The self-heterodyne interferometer is a powerful tool for characterizing laser noise [11]. In a typical arrange-

ment, the heterodyne circuit outputs a current $I(t)$ (or normalized current $i(t)$, as defined below) containing the noise signal. The resulting power spectral density, $S_i(f)$, provides a convenient proxy for laser field and frequency fluctuations, $S_E(f)$ and $S_{\delta\nu}(f)$, although the correspondence is not one-to-one. In this section, we derive these three functions and show how they are related, focusing on the regime of weak frequency noise. While many of the results in this section have been obtained previously, we re-derive them here to establish a common framework and notation. We then apply our results to two types of noise affecting atomic qubit experiments: white noise and servo bumps. This analysis forms the starting point for the master equation calculations that follow.

The Rabi oscillations of a qubit are driven by a classical laser field, which we define as

$$\mathbf{E}(t) = \frac{\hat{\mathbf{e}}E_0}{2}e^{i[2\pi\nu t+\phi(t)]} + \text{c.c.}, \tag{1}$$

where c.c. stands for complex conjugate. Here we assume the polarization vector $\hat{\mathbf{e}}$ is real, although E_0 may be complex. Fluctuations of the laser field are the main source of decoherence in current atomic qubit experiments, and are the focus of the present work. The fluctuations may occur in any of the field parameters, $\hat{\mathbf{e}}$, E_0, or ϕ, where the latter is the phase of the drive. For lasers of interest, the fluctuations predominantly occur in the phase variable. In this work, we therefore ignore noise in the polarization vector and we only briefly consider relative intensity noise (RIN), where the intensity is proportional to E_0^2. Instead, we focus mainly on the fluctuations of $\phi(t)$. Alternatively, and equivalently, we may consider fluctuations of the frequency, $\nu(t) = \nu_0 + \delta\nu(t)$, which are related to phase fluctuations through the relation

$$\phi(t) = \int_{t_0}^{t_0+t} 2\pi\delta\nu(t')dt', \tag{2}$$

where t_0 is a reference time.

The fluctuations of $\delta\nu(t)$ [or $\phi(t)$] have a direct influence on the Rabi oscillations, and must therefore be carefully characterized. A compact description of a general fluctuating variable $X(t)$ is given by its autocorrelation function, defined as

$$R_X(\tau) = \langle X(t)X(t+\tau)\rangle \equiv \lim_{T\to\infty}\frac{1}{2T}\int_{-T}^{T} X(t)X(t+\tau)dt. \tag{3}$$

According to the Weiner-Khintchine theorem, the autocorrelation function of $X(t)$ is related to its noise power spectrum by the Fourier transform,

$$S_X(f) = \int_{-\infty}^{\infty} R_X(\tau)e^{-i2\pi f\tau}d\tau, \tag{4}$$

and its inverse transform,

$$R_X(\tau) = \int_{-\infty}^{\infty} S_X(f)e^{i2\pi f\tau}df, \tag{5}$$

where in this work, we consider two-sided power spectra.

The main goal of this work is to characterize the noise spectrum of $E(t)$. However, $S_E(f)$ (also called the laser lineshape) cannot be measured directly, due to the high frequency of the carrier. We must therefore transduce the power spectrum to lower frequencies. Here, we consider the self-heterodyne transduction technique, in which the laser field is split, modified, and recombined to perform interferometry measurements. The resulting signal is read out as a photocurrent containing a direct imprint of the underlying noise spectrum. For the dimensionless photocurrent $i(t)$, which we define below, the self-heterodyne power spectrum is denoted $S_i(f)$.

In this section, we derive the interrelated power spectra of $S_E(f)$ and $S_i(f)$, which are in turn functions of the underlying noise spectrum $S_{\delta\nu}(f)$ [or $S_\phi(f)$]. To perform noisy gate simulations, as discussed in later sections, one would like to use actual self-heterodyne experimental data to characterize the underlying noise spectra. In principle, such a deconvolution cannot be implemented exactly [12]. However, we will show that reliable results for the noise power may indeed be obtained, particularly for lasers with very low noise levels, such as the locked and filtered lasers used in recent qubit experiments.

A. Laser Lineshape

The autocorrelation function for the laser field is defined as

$$R_E(\tau) = \langle E(t)E(t+\tau)\rangle. \tag{6}$$

This function contains information about both the carrier signal, centered at frequency ν_0, and the fluctuations, which are typically observed as a fundamental broadening of the carrier peak. Additional features of importance for qubit experiments include structures away from the peak that may be caused by the laser locking and filtering circuitry, such as the "servo bump," discussed in detail below.

The time average in Eq. (6) has been evaluated by a number of authors. For completeness, we summarize these derivations here, following the approach of Ref. [13]. Let us begin by assuming the noise process is strongly stationary, so that Eq. (6) does not depend on t; for simplicity, we set $t = 0$. Using Eqs. (1) and (6) and trigonometric identities, we then have

$$\begin{aligned} R_E(\tau) = &\left\{\frac{E_0^2}{4}e^{i[2\pi\nu_0\tau+\phi(\tau)+\phi(0)]} + \text{h.c.}\right\} \\ &+ \frac{|E_0|^2}{2}\Big\{\cos(2\pi\nu_0\tau)\langle\cos[\phi(\tau)-\phi(0)]\rangle \\ &\qquad - \sin(2\pi\nu_0\tau)\langle\sin[\phi(\tau)-\phi(0)]\rangle\Big\}. \end{aligned} \tag{7}$$

We then assume the phase difference $\Phi(\tau) \equiv \phi(\tau) - \phi(0)$ to be a gaussian random variable centered at $\Phi(\tau) = 0$,

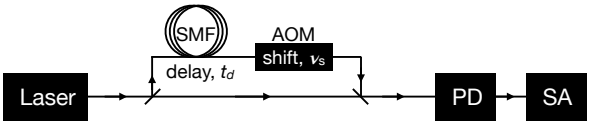

FIG. 1. Heterodyne setup. The laser signal is split equally between two paths. One path passes through a single-mode fiber (SMF), where it is delayed by time t_d. It then passes through an acousto-optic modulator (AOM), where its frequency is shifted by ν_s. The interfering signals are combined and measured by a photodiode (PD), and finally processed through a spectrum analyzer (SA).

with probability distribution

$$p(\Phi) = \frac{1}{\sigma_\Phi \sqrt{2\pi}} e^{-\Phi^2/2\sigma_\Phi^2},$$

and variance $\overline{\Phi^2} = \sigma_\Phi^2$. Here, the bar denotes an ensemble average. According to the ergodic theorem, ensemble and time averages should give the same result, so that

$$\sigma_\Phi^2(\tau) = \langle [\phi(\tau) - \phi(0)]^2 \rangle = 2R_\phi(0) - 2R_\phi(\tau), \qquad (8)$$

where we note that

$$\langle \phi^2(0) \rangle = \langle \phi^2(\tau) \rangle = R_\phi(0).$$

Again, making use of the ergodic theorem, we have

$$\langle \cos(\Phi) \rangle = e^{-\sigma_\Phi^2/2} \quad \text{and} \quad \langle \sin(\Phi) \rangle = 0, \qquad (9)$$

which is also known as the moment theorem for gaussian random variables. Finally we note that only biased variables like $\phi(\tau) - \phi(0)$ are gaussian. An unbiased variable like $\phi(\tau) + \phi(0)$ is simply a random phase, for which $\langle \cos[\phi(\tau) + \phi(0)] \rangle = \langle \sin[\phi(\tau) + \phi(0)] \rangle = 0$. Combining these facts, we obtain the important relation [14]

$$R_E(\tau) = \frac{|E_0|^2}{2} \cos(2\pi\nu_0\tau) \exp\left[R_\phi(\tau) - R_\phi(0)\right]. \qquad (10)$$

Note that since ϕ can take any value, $R_\phi(0)$ does not have physical significance on its own; only the difference $R_\phi(\tau) - R_\phi(0)$ is meaningful.

Another useful form for Eq. (10) can be obtained from the relation $2\pi\delta\nu(t) = \partial\phi/\partial t$, together with Eq. (4) and the stationarity of $R_\phi(t)$, yielding

$$S_{\delta\nu}(f) = f^2 S_\phi(f). \qquad (11)$$

Applying trigonometric identities, we then obtain the following, well-known results for the laser lineshape [12]:

$$R_E(\tau) = \frac{|E_0|^2}{2} \cos(2\pi\nu_0\tau) \exp\left[-2\int_{-\infty}^{\infty} S_{\delta\nu}(f) \frac{\sin^2(\pi f\tau)}{f^2}\, df\right], \qquad (12)$$

and

$$S_E(f) = \frac{|E_0|^2}{2} \int_{-\infty}^{\infty} \cos(2\pi f\tau) \cos(2\pi\nu_0\tau) \exp\left[-2\int_{-\infty}^{\infty} S_{\delta\nu}(f') \frac{\sin^2(\pi f'\tau)}{(f')^2}\, df'\right] d\tau. \qquad (13)$$

It is common to adopt a lineshape that is centered at zero frequency; henceforth, we therefore set $\nu_0 = 0$. We note that $S_E(f)$ is properly normalized here, with $\int_{-\infty}^{\infty} S_E(f) df = |E_0|^2/2$. Thus, fluctuations that broaden the lineshape also reduce the peak height.

Some additional interesting results follow from Eq. (13). First, in the absence of noise [$S_{\delta\nu} = 0$], we see that the laser lineshape immediately reduces to an unbroadened carrier signal: $S_E(f) = (|E_0|^2/2)\delta(f)$. Second, when $S_{\delta\nu}$ is nonzero but small, as typical for a locked and filtered laser, the exponential term in Eq. (13) may be expanded to first order, yielding [**?**]

$$2S_E(f)/|E_0|^2 \approx [1 - R_\phi(0)]\delta(f) + S_\phi(f). \qquad (14)$$

This approximation is generally very good, but breaks down in the asymptotic limit $\tau \to \infty$ of the τ integral, and therefore the limit $f \to 0$. To see this, we note that $\sin^2(\pi f\tau)$ may be replaced by its average value of 1/2 in the integral; for nonvanishing values of $S_{\delta\nu}(0)$, the argument of the exponential then diverges. To estimate the frequency f_x, below which Eq. (14) breaks down, we set the argument of the exponential in Eq. (14) to 1/2:

$$2\int_{f_x}^{\infty} \frac{S_{\delta\nu}(f)}{f^2} df \approx \frac{1}{2}. \qquad (15)$$

This criterion clearly depends on the noise spectrum.

To conclude, we note that for some analytical calculations (such as the servo-bump analysis, described below), it may be convenient or pedagogical to separate the noise spectrum into distinct components: $S_{\delta\nu}(f) = S_{\delta\nu,1}(f) + S_{\delta\nu,2}(f)$, corresponding to different physical noise mechanisms. From Eq. (12), the resulting lineshapes can then be written as

$$R_E(\tau) = 2|E_0|^{-2} R_{E,1}(\tau) R_{E,2}(\tau), \qquad (16)$$

where $R_{E,1}(\tau)$ and $R_{E,2}(\tau)$ are the autocorrelation func-

tions corresponding to $S_{\delta\nu,1}(f)$ and $S_{\delta\nu,2}(f)$. Applying the Fourier convolution theorem, we obtain

$$S_E(f) = 2|E_0|^{-2}\int_{-\infty}^{\infty} S_{E,1}(f-f')S_{E,2}(f')df'. \quad (17)$$

B. Self-Heterodyne Spectrum

We consider the self-heterodyne optical circuit shown in Fig. 1. As depicted in the diagram, one of the paths is delayed by time t_d, through a long optical fiber, and then shifted in frequency by ν_s, by means of an acousto-optic modulator. Here, the delay loop allows us to interfere phases at different times, while the frequency shift provides a beat tone that is readily accessible to electronic measurements, since it occurs at submicrowave frequencies, $\nu_s \approx 100$ MHz. The two beams are then recombined and the total intensity is measured by a photodiode, using conventional measurement techniques.

For simplicity, we assume the laser signal is split equally between the two paths, although unequal splittings may also be of interest [**?**]. The recombined field amplitude is defined as

$$E(t) = \frac{E_0}{2}\Big\{\exp[i2\pi\nu_0 t + i\phi(t)] + \exp[i2\pi(\nu_0+\nu_s)(t-t_d) + i\phi(t-t_d)]\Big\} + \text{c.c.} \quad (18)$$

The output current of the photodiode is then proportional to $E^2(t)$. For convenience, we consider instead a dimensionless photocurrent $i(t)$ given by

$$i(t) = \frac{1}{2}\Big\{\cos[2\pi\nu_0 t + \phi(t) + \alpha] + \cos[2\pi(\nu_0+\nu_s)(t-t_d) + \phi(t-t_d) + \alpha]\Big\}^2, \quad (19)$$

where $E_0 = |E_0|e^{i\alpha}$. The corresponding autocorrelation function is defined as

$$R_i(\tau) = \langle i(t)i(t+\tau)\rangle. \quad (20)$$

The evaluation of $R_i(\tau)$ is greatly simplified by noting that cosine terms with ν_0 in their argument average to zero in a physically realistic measurement. Again making use of the fact that unbiased variables like $\phi(\tau)+\phi(0)$ are random phases and nongaussian, we find that

$$R_i(\tau) = 4 + 2\langle\cos[2\pi\nu_s\tau + \phi(t) - \phi(t-t_d) - \phi(t+\tau) + \phi(t+\tau-t_d)]\rangle. \quad (21)$$

Taking the same approach as in the derivation of $R_E(\tau)$, we take $\Phi' = \phi(t) - \phi(t-t_d) - \phi(t+\tau) + \phi(t+\tau-t_d)$ to be a gaussian random variable centered at zero, and apply the gaussian moment relations,

$$\langle\cos(\Phi')\rangle = e^{-\sigma^2_{\Phi'}/2} \quad \text{and} \quad \langle\sin(\Phi')\rangle = 0, \quad (22)$$

where

$$\sigma^2_{\Phi'} = \langle[\phi(t) - \phi(t-t_d) - \phi(t+\tau) + \phi(t+\tau-t_d)]^2\rangle. \quad (23)$$

In this way we obtain

$$R_i(\tau) = 4 + 2\cos(2\pi\nu_s\tau) \times \exp[2R_\phi(\tau) + 2R_\phi(t_d) - 2R_\phi(0) - R_\phi(\tau-t_d) - R_\phi(\tau+t_d)]. \quad (24)$$

Here, the cosine function represents the beat tone, and the noise information is reflected in its amplitude. It can be seen that the corresponding power spectrum, $S_i(f)$, includes a central peak, $\delta(f)$, which contains no information about the laser noise, and two broadened but identical satellite peaks, centered at $f = \pm\nu_s$. We now recenter $R_i(\tau)$ at one of the satellite peaks, as consistent with typical self-heterodyne measurements, such that

$$R_i(\tau) \to R_i(\tau) = \exp[2R_\phi(\tau) + 2R_\phi(t_d) - 2R_\phi(0) - R_\phi(\tau-t_d) - R_\phi(\tau+t_d)]. \quad (25)$$

Applying trigonometric identities, we then obtain

$$R_i(\tau) = \exp\left[-8\int_{-\infty}^{\infty} S_{\delta\nu}(f)\frac{\sin^2(\pi f\tau)\sin^2(\pi f t_d)}{f^2}df\right], \quad (26)$$

and

$$S_i(f) = \int_{-\infty}^{\infty}\cos(2\pi f\tau)R_i(\tau). \quad (27)$$

We note that the self-heterodyne peak defined in this way is normalized such that $\int_{-\infty}^{\infty} S_i(f)df = R_i(0) = 1$.

In the absence of noise [$S_{\delta\nu} = 0$], we see from Eqs. (26) and (27) that the self-heterodyne power spectrum reduces to the bare carrier: $S_i(f) = \delta(f)$. For nonzero but small $S_{\delta\nu}$, we can expand the exponential in Eq. (26), as was done in Eq. (14), to obtain

$$S_i(f) \approx \big[1 + 2R_\phi(t_d) - 2R_\phi(0)\big]\delta(f) + 4\sin^2(\pi f t_d)S_\phi(f). \quad (28)$$

The second term in this expression is closely related to the envelope-ratio power spectral density described in Ref. [**?**], following on the earlier work of Ref. [**?**], and provides a theoretical basis for the former.

As in the derivation of Eq. (14), the expansion leading to Eq. (28) breaks down at low frequencies. However, the well-known "scallop" features in the power spectrum are seen to arise from the factor $\sin^2(\pi f t_d)$. This result clarifies the relation between the self-heterodyne signal, the underlying laser noise, and the laser lineshape. The latter relation is given by

$$E_0^2 S_i(f) \approx 2\sin^2(\pi f t_d)S_E(f), \quad (29)$$

where we have omitted the central carrier peak.

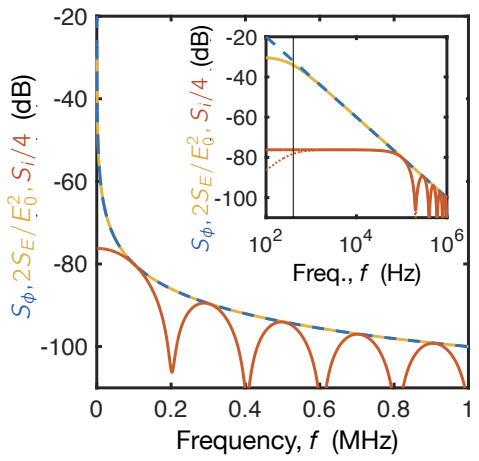

FIG. 2. White-noise power spectral densities, $S_\phi(f)$ (blue), $2S_E(f)/E_0^2$ (gold), and $S_i(f)/4$ (red), defined in Eqs. (32), (35), and (38), respectively, for noise strength $h_0 = 100$ Hz. Here we have omitted the δ-function peak in $S_i(f)$. The inset shows the same quantities plotted on a logarithmic frequency scale. An approximate form for $S_i/4$ (red, dotted) is obtained from Eq. (29). The cutoff f_x (vertical black), defined in Eq. (15), indicates the frequency where Eq. (14) begins to fail.

To conclude, we again consider the possibility that the noise spectrum may be separated into distinct components, $S_{\delta\nu}(f) = S_{\delta\nu,1}(f) + S_{\delta\nu,2}(f)$. As for the laser lineshape, the self-heterdyne autocorrelation function may then be written as

$$R_i(\tau) = R_{i,1}(\tau)R_{i,2}(\tau), \tag{30}$$

yielding the combined power spectrum

$$S_i(f) = \int_{-\infty}^{\infty} S_{i,1}(f - f')S_{i,2}(f')df'. \tag{31}$$

C. White Noise

The self-heterodyne laser noise measurements, reported below, are well described by a combination of white noise and a Gaussian servo bump. We now obtain analytical results for the $S_E(f)$ and $S_i(f)$ power spectra, for these two noise models. The results for white noise are well-known [**?**]. However we reproduce them here for completeness.

The underlying noise spectrum for white noise is given by

$$S_{\delta\nu} = h_0 \qquad \text{or} \qquad S_\phi(f) = \frac{h_0}{f^2}. \tag{32}$$

Note that it is common to use a one-sided noise spectrum for such calculations; however we use a two-sided spectrum here. Our results may therefore differ by a factor of 2 from others reported in the literature. The most straightforward calculation of $R_\phi(\tau)$, from Eq. (5), immediately encounters a singularity. We therefore proceed by calculating $R_E(\tau)$ from Eq. (12). Setting $\nu_0 = 0$, to center the power spectrum, then gives

$$R_E(\tau) = \frac{E_0^2}{2} e^{-2\pi^2 h_0 |\tau|}. \tag{33}$$

From Eq. (10), we can identify

$$R_\phi(\tau) - R_\phi(0) = -2\pi^2 h_0 |\tau|, \tag{34}$$

where the singularity has now been absorbed into $R_\phi(0)$. Solving for the laser lineshape yields

$$S_E(f) = \frac{E_0^2 h_0/2}{f^2 + (\pi h_0)^2}, \tag{35}$$

for which the full-width-at-half-maximum (FWHM) linewidth is $2\pi h_0$. Away from the carrier peak, which is very narrow for a locked and well-filtered laser, we find

$$2S_E(f)/E_0^2 \approx \frac{h_0}{f^2} = S_\phi(f), \tag{36}$$

as consistent with Eq. (14).

We can also evaluate the self-heterodyne autocorrelation function, Eq. (25), obtaining

$$R_i(\tau) = \exp\left[-2\pi^2 h_0 (2t_d + 2|\tau| - |\tau - t_d| - |\tau + t_d|\right], \tag{37}$$

and the corresponding power spectrum,

$$S_i(f) = \frac{2h_0}{f^2 + (2\pi h_0)^2} + e^{-4\pi^2 h_0 t_d}\left\{\delta(f) - \frac{2h_0}{f^2 + (2\pi h_0)^2}\left[\cos(2\pi f t_d) + \frac{2\pi h_0}{f}\sin(2\pi f t_d)\right]\right\}. \tag{38}$$

It is interesting to visualize the results and approximations employed above. In Fig. 2 we plot the white-noise power spectral densities $S_\phi(f)$, $S_E(f)$, and $S_i(f)$ corresponding to Eqs. (32), (35)], and (38), on both linear and logarithmic scales, for the noise amplitude $h_0 = 100$ Hz. In the inset, we also plot the approximate relation between $S_i(f)$ and $S_E(f)$ given by Eq. (29), which clarifies how self-heterodyne measurements may be used to characterize the laser noise. Here, we also plot the crossover frequency f_x from Eq. (15), below which the approximations in Eq. (29) begin to fail. For the case of white noise, this expression can be evaluated analytically, giving $f_x = 4h_0$.

The scallop features in Fig. 2 are caused by beating between the interfering fields in the self-heterodyne circuit. We note that, in principle, the fine-scale noise features present in $S_\phi(f)$ or $S_E(f)$ are inherited by $S_i(f)$. However some features are obscured by the scallops, which suppress the measured signal at frequency intervals of $\Delta f = 1/t_d$.

D. Servo Bump

Laser are commonly stabilized by locking to narrow-linewidth reference cavities. This feedback system is called a servo loop [**?**], and the finite bandwidth of the feedback loop induces peaks in $S_{\delta\nu}(f)$ called servo bumps, which are typically shifted above and below the central peak by frequencies on the order of 1 MHz. We find that experimental servo bumps have approximately gaussian shapes. In fact, we find that the full noise model is well described by a gaussian servo bump combined with white noise, as defined by

$$\begin{aligned} S_{\delta\nu}(f) &= h_0 + h_g \exp\left[-\frac{(f-f_g)^2}{2\sigma_g^2}\right] + h_g \exp\left[-\frac{(f+f_g)^2}{2\sigma_g^2}\right] \\ &= h_0 + \frac{s_g f_g^2}{\sqrt{8\pi}\sigma_g} \exp\left[-\frac{(f-f_g)^2}{2\sigma_g^2}\right] + \frac{s_g f_g^2}{\sqrt{8\pi}\sigma_g} \exp\left[-\frac{(f+f_g)^2}{2\sigma_g^2}\right]. \end{aligned} \tag{39}$$

Here, h_g is the bump's height and σ_g is its width, with a FWHM given by $\sqrt{\ln 4}\,\sigma_g$.

In the second line of Eq. (39), we use an alternative expression for the bump height, in terms of its total, dimensionless phase-noise power, $s_g = \int_{-\infty}^{\infty} S_{\phi,g}(f)df$, where the subscript g refers to the gaussian noise components. We use this expression in the simulations described below, to explore the effects of different bump shapes. To perform the s_g conversion here, we note that $S_{\phi,g}(f)$ is actually singular at $f = 0$, causing its integral to diverge. We can regularize this divergence by assuming that the servo bump is narrow (which appears to be true in many experiments), and by making the substitution

$$S_\phi(f) = S_{\delta\nu}(f)/f^2 \approx S_{\delta\nu}(f)/f_g^2, \tag{40}$$

yielding

$$s_g \approx \sqrt{8\pi}\sigma_g h_g/f_g^2, \tag{41}$$

which is the form used in Eq. (39). We can think of this expression as describing the noise power in just the servo bump, and not the low-frequency portion of the spectrum. We emphasize that the latter is not ignored – but it is subsumed into the white noise, which we treat separately.

We first consider just the gaussian term in Eq. (39), setting $h_0 = 0$. Fourier transforming Eq. (40), we obtain

$$R_\phi(\tau) \approx s_g \cos(2\pi f_g \tau) e^{-2\pi^2\sigma_g^2\tau^2}. \tag{42}$$

Thus for $s_g \ll 1$, Eq. (14) gives

$$\begin{aligned} 2S_E(f)/E_0^2 \approx \delta(f) &+ \frac{h_g}{f_g^2}\exp\left[-\frac{(f-f_g)^2}{2\sigma_g^2}\right] \\ &+ \frac{h_g}{f_g^2}\exp\left[-\frac{(f+f_g)^2}{2\sigma_g^2}\right], \end{aligned} \tag{43}$$

and Eq. (28) gives

$$\begin{aligned} S_i(f) \approx \delta(f) &+ \frac{4h_g}{f_g^2}\sin^2(\pi f t_d)\exp\left[-\frac{(f-f_g)^2}{2\sigma_g^2}\right] \\ &+ \frac{4h_g}{f_g^2}\sin^2(\pi f t_d)\exp\left[-\frac{(f+f_g)^2}{2\sigma_g^2}\right]. \end{aligned} \tag{44}$$

The white noise component of $S_{\delta\nu}(f)$ can now be included, obtaining Eqs. (17) and (31), yielding

$$S_E(f) = 2E_0^{-2}\int_{-\infty}^{\infty} S_{E,w}(f-f')S_{E,g}(f')df', \tag{45}$$

$$S_i(f) = \int_{-\infty}^{\infty} S_{i,w}(f-f')S_{i,g}(f')df', \tag{46}$$

where the subscripts w and g refer to white and gaussian power spectra, which have already been computed. We solve these integrals, approximately, by noting that a convolution between two peaks, with very different widths, is dominated by the wider peak. We further note that, for the lasers of interest here, the servo bump is much wider than the white-noise Lorentzian peak, which is in turn much wider than a delta function. Hence, we find that

$$\begin{aligned} 2S_E(f)/E_0^2 \approx \frac{h_0}{f^2+(\pi h_0)^2} &+ \frac{h_g}{f_g^2}\exp\left[-\frac{(f-f_g)^2}{2\sigma_g^2}\right] \\ &+ \frac{h_g}{f_g^2}\exp\left[-\frac{(f+f_g)^2}{2\sigma_g^2}\right], \end{aligned} \tag{47}$$

and

$$\begin{aligned} S_i(f) \approx \frac{2h_0}{f^2+(2\pi h_0)^2} &+ e^{-4\pi^2 h_0 t_d}\left\{\delta(f)\right. \\ &\left. - \frac{2h_0}{f^2+(2\pi h_0)^2}\left[\cos(2\pi f t_d) + \frac{2\pi h_0}{f}\sin(2\pi f t_d)\right]\right\} \\ &+ \frac{4h_g}{f_g^2}\sin^2(\pi f t_d)\exp\left[-\frac{(f-f_g)^2}{2\sigma_g^2}\right] \\ &+ \frac{4h_g}{f_g^2}\sin^2(\pi f t_d)\exp\left[-\frac{(f+f_g)^2}{2\sigma_g^2}\right]. \end{aligned} \tag{48}$$

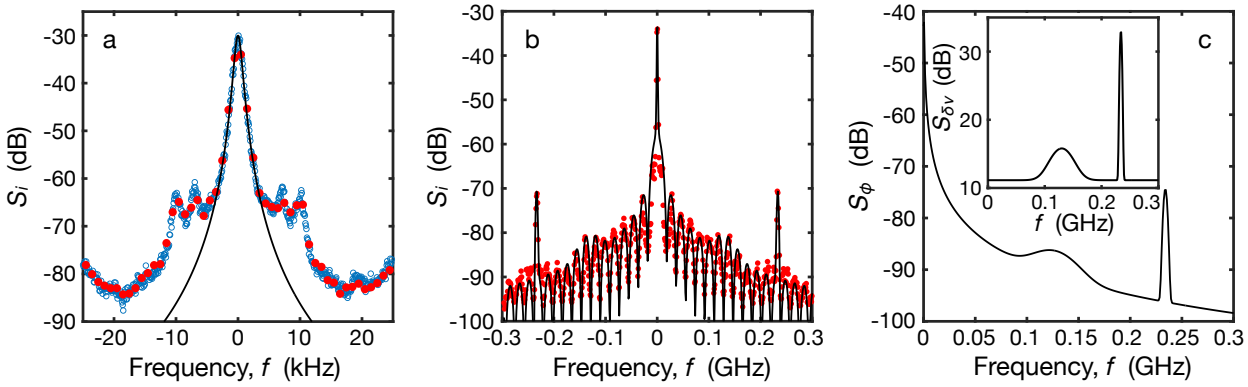

FIG. 3. 1040 nm solid-state Ti:Sa laser self-heterodyne data with fits to noise models. (a) Self-heterodyne power spectral density, obtained in a 50 kHz frequency window with RBW = 100 Hz (open blue circles) and in a 600 kHz window with RBW = 300 Hz (closed red markers). An optical delay fiber of 11 km is used for both data sets, corresponding to a delay time of $t_d = 5.445 \times 10^{-5}$ s. The data are shifted horizontally to center their peaks at zero frequency, and the peak data are then fit to Eq. (49) (black line), obtaining $\alpha = 5/2$ and $\sigma = 240$ Hz. The data are finally renormalized (i.e., shifted vertically) to ensure the correct total power, as described in the main text. (b) Same red data set as (a), plotted over a wider frequency window. The data are fit to Eq. (48), including white noise and two gaussian servo bumps, obtaining $h_0 = 13$ Hz^2/Hz, $h_{g1} = 2.0 \times 10^3$ Hz^2/Hz, $\sigma_{g1} = 1.5$ kHz, $f_{g1} = 234$ kHz, $h_{g2} = 25$ Hz^2/Hz, $\sigma_{g2} = 18$ kHz, and $f_{g2} = 130$ kHz. (c) Phase and frequency power spectral densities, $S_\phi(f)$ and $S_{\delta\nu}(f)$ (inset), resulting from the fitting.

In the following section, we apply these equations as fitting forms for experimental self-heterodyne data.

III. LASER CHARACTERIZATION

To help visualize these results, we now characterize a strongly filtered solid-state Ti:Sa laser used in qubit applications. In Fig. 3(a), we plot two experimental data sets from the same laser (red and blue markers). We find that the central peak is broadened more significantly than the resolution bandwidth (RBW) settings of the spectrum analyzer. The corresponding linewidths are approximately equal, despite their different RBW, suggesting that RBW is not the only source of broadening.

Although the central peak does not exhibit a clear characteristic form, we find that that it is well described by

$$S_{i,\mathrm{peak}}(f) = \frac{s_p \sigma^{2\alpha-1}}{(f^2 + \pi^2\sigma^2)^\alpha}. \tag{49}$$

Fitting the data to this form yields $\alpha = 5/2$ and $\sigma = 240$ Hz. The corresponding FWHM is 850 Hz, which is indeed several times larger than the RBW of the measurements. Integrating Eq. (49) over frequency yields $4s_p/3\pi^4$. The data are therefore shifted vertically in Fig. 3(a) to give the correct normalization, $\int_{-\infty}^{\infty} S_i(f)df = 1$.

After this normalization step, the self-heterodyne data away from the peak are fit to Eq. (48), where we introduce two distinct servo bumps, obtaining the result shown in Fig. 3(b) (black line). The fitting parameters are given by $h_0 = 13$ Hz^2/Hz for the white noise, and $h_{g1} = 2.0 \times 10^3$ Hz^2/Hz, $\sigma_{g1} = 1.5$ kHz, $f_{g1} = 234$ kHz, $h_{g2} = 25$ Hz^2/Hz, $\sigma_{g2} = 18$ kHz, and $f_{g2} = 130$ kHz for the servo bumps. The corresponding power spectral densities for the noise are plotted in Fig. 3(c). We can use these results to determine the fractional noise power in different components of the S_ϕ spectrum For the first servo bump, we obtain the fractional power $s_{g1} = 0.00027$, and for the second servo bump, we obtain the fractional power $s_{g2} = 0.00013$. Together, these represent a small but non-negligible fraction of the total laser power.

IV. DENSITY MATRIX SOLUTIONS FOR RABI OSCILLATIONS

In this section, we compute the density matrix of a qubit undergoing Rabi oscillations driven by a laser with frequency noise. The calculation involves taking an average over all possible noise realizations. In Sec. IV A, we perform a Fourier expansion of a generic Gaussian noise process, which is incorporated into the master equation calculation of Sec. IV B, and is used again in the numerical simulations of Sec. V. In Sections IV C and IV D, we use our master equation results to compute one and two-photon gate fidelities for the Rabi oscillations.

A. Time-Series Expansion of the Laser Noise

A real, fluctuating Gaussian process $X(t)$, with zero mean and variance σ_X^2, can generally be expressed as a

Fourier time series:

$$X(t) = \sum_{j=1}^{\infty} x_j \cos(2\pi f_j t + \varphi_j), \tag{50}$$

where $f_j = j\Delta f$. Here, we have defined $X(0) = 0$ for convenience. The random variables x_j can be selected as Rayleigh-distributed random values [**?**], while the random variables φ_j are uniformly distributed over $[0, 2\pi]$.

We can compute the variance of $X(t)$ as

$$\sigma_X^2 = \left\langle \sum_{j,k} x_j x_k \cos(2\pi f_j t + \varphi_j)\cos(2\pi f_k t + \varphi_k) \right\rangle, \tag{51}$$

where an average is taken over the various random variables. Since these variables are assumed to be statistically independent, the double sum vanishes, except for the case $j = k$. Hence,

$$\sigma_X^2 = \sum_{j=1}^{\infty} \langle x_j^2 \rangle / 2. \tag{52}$$

The variance is also related to the same-time autocorrelation function, defined in Eq. (VII), such that

$$\sigma_X^2 = R_X(0) = \int_0^{\infty} S_X^{\text{1-sided}}(f) df = \sum_{j=1}^{\infty} S_{X,j}^{\text{1-sided}} \Delta f, \tag{53}$$

where we have used the one-sided version of the noise spectral density function $S_X(f)$. We have also converted the integral to a series representation, with $S_{X,j} = S_X(f_j)$.

Comparing Eqs. (52) and (53), we note the correspondence

$$\langle x_j^2 \rangle \leftrightarrow 2 S_{X,j}^{\text{1-sided}} \Delta f. \tag{54}$$

To generate time traces of $X(t)$, it is then standard practice to make the following replacement for the random variable x_j in Eq. (50) [**?**]:

$$x_j \to \sqrt{2 S_{X,j}^{\text{1-sided}} \Delta f} = 2\sqrt{S_{X,j}^{\text{2-sided}} \Delta f}. \tag{55}$$

Defined in this way, x_j is deterministic rather than random. The resulting time trace $X(t)$ inherits the correct statistical properties of x_j. Although this procedure cannot account for all random behavior of $X(t)$ [**?**], it successfully describes most behavior.

The method described above is used to generate random time traces in our numerical simulations, as described below in Sec. V A. These simulations incorporate time traces of the laser phase fluctuations, defined as

$$\phi(t) = \sum_{j=1}^{\infty} 2\sqrt{S_{\phi}^{\text{2-sided}}(f_j)\Delta f} \cos(2\pi f_j t + \varphi_j). \tag{56}$$

Here, we note that, while time-series amplitude coefficients have been replaced by their deterministic averages, the random phases φ_j must still be chosen from the uniform distribution $[0, 2\pi]$. In the following section, we incorporate time traces of the laser frequency fluctuations, defined as

$$\delta\nu(t) = \frac{1}{2\pi}\frac{d\phi}{dt} = \sum_{j=1}^{\infty} \delta\nu_j \sin(2\pi f_j t + \varphi_j), \tag{57}$$

where

$$\delta\nu_j = -2\sqrt{S_{\delta\nu}^{\text{2-sided}}(f_j)\Delta f}, \tag{58}$$

and we make use of the relation $S_{\delta\nu}^{\text{2-sided}}(f) = f^2 S_{\phi}^{\text{2-sided}}(f)$. For brevity, we henceforth drop the superscript "2-sided."

B. Time-Series Master Equation

We consider the two-level system $\{|g\rangle, |e\rangle\}$, with corresponding energy levels E_g and E_e, and qubit energy $h\nu_0 = E_e - E_g$. The Hamiltonian for a resonantly driven qubit, by a monochromatic laser with angular frequency ν_0 and angular Rabi frequency Ω_0 is then given by

$$\begin{aligned} H = {} & \frac{h\nu_0}{2}(|e\rangle\langle e| - |g\rangle\langle g|) \\ & + \hbar\Omega_0 \cos(2\pi\nu_0 t)\left[e^{i\phi(t)}|e\rangle\langle g| + e^{-i\phi(t)}|g\rangle\langle e|\right], \end{aligned} \tag{59}$$

where we have explicitly included phase fluctuations $\phi(t)$. Moving to a rotating frame defined by $U(t) = \exp[i\pi\nu_0 t(|e\rangle\langle e| - |g\rangle\langle g|)]$ and applying a rotating wave approximation (RWA), we obtain the transformed Hamiltonian

$$\begin{aligned} H' &\approx \frac{\hbar\Omega_0}{2}\left[e^{i\phi(t)}|e\rangle\langle g| + e^{-i\phi(t)}|g\rangle\langle e|\right], \\ &= \frac{\hbar\Omega_0}{2}[\cos\phi(t)\,\sigma_x + \sin\phi(t)\,\sigma_y], \end{aligned} \tag{60}$$

where the Pauli matrices are defined as $\sigma_x = |g\rangle\langle e| + |e\rangle\langle g|$, $\sigma_y = i|g\rangle\langle e| - i|e\rangle\langle g|$, and $\sigma_z = |g\rangle\langle g| - |e\rangle\langle e|$.

In Eqs. (59) and (60), the axis of Rabi rotations shifts with the fluctuating phase $\phi(t)$. Although this description captures the physics of the problem, it is inconvenient for our calculations. We therefore consider a frame that follows the fluctuating phase, in which the rotation axis is fixed [**?**]. This fluctuating frame is defined by the transformation $U_\varphi(t) = \text{diag}[e^{-i\varphi/2}, e^{i\varphi/2}]$, yielding the Hamiltonian

$$\begin{aligned} H'' &\approx \frac{\hbar\Omega_0}{2}\sigma_x - \frac{\hbar(d\phi/dt)}{2}\sigma_z \\ &= \frac{\hbar\Omega_0}{2}\sigma_x - \frac{h\delta\nu(t)}{2}\sigma_z \\ &= \frac{\hbar\Omega_0}{2}\sigma_x - \sum_{j=1}^{\infty}\frac{h\delta\nu_j}{2}\sin(2\pi f_j t + \varphi_j)\sigma_z, \end{aligned} \tag{61}$$

where we make use of Eq. (57), and the only approximation employed is the standard RWA in Eq. (60).

In Eq. (61), we have moved to a frame where Ω_0 now represents the quantizing field, and where $\delta\nu_j$ represents a Rabi driving term, applied simultaneously at multiple frequencies. To formalize this correspondence, we move to the frame where Ω_0 points towards the north pole of the Bloch sphere, as defined by the transformation $U = \exp[-i(\pi/4)\sigma_y]$, obtaining

$$H''' \approx \frac{\hbar\Omega_0}{2}\sigma_z + \sum_{j=1}^{\infty}\frac{h\delta\nu_j}{2}\sin(2\pi f_j t + \varphi_j)\sigma_x. \tag{62}$$

For simplicity, we drop the primed notation on H''' in the following derivations.

We now solve for the time evolution of the density operator, for a two-level system governed by Eq. (62):

$$\hbar\frac{d\rho}{dt} = i[\rho, H]. \tag{63}$$

Although Eq. (62) has the standard form of a Rabi rotation, we note that conventional Rabi techniques are not applicable here, because in the frame of Eq. (62), the initial state of the system is along the driving axis of the Bloch sphere ($\hat{x}$), as discussed below. As such, the time evolution arises entirely from counterrotating terms in Eq. (62), rather than co-rotating terms. (Note that counterrotating and co-rotating refer, here, to the $\delta\nu_j$ fluctuations, not the original Rabi drive.) Moreover, as will become apparent below, it is desirable to consider perturbative corrections to $\rho(t)$, which are of order $\mathcal{O}[\delta\nu_j^2]$ in the frequency fluctuations.

To construct a perturbation theory, we first note that $2\pi\delta\nu_j$ is typically smaller than Ω_0, allowing us to define the dimensionless small parameter, $\delta_j = 2\pi\delta\nu_j/\Omega_0 \lesssim 1$. Defining $\omega_j = 2\pi f_j$, the Hamiltonian becomes

$$\frac{H}{\hbar\Omega_0} = \frac{\sigma_z}{2} + \sum_{j=1}^{\infty}\delta_j\frac{\sigma_x}{2}\sin(\omega_j t + \varphi_j). \tag{64}$$

We can then solve the density matrix by expanding in terms of our small parameter,

$$\begin{aligned}\rho &= \rho_0 + \rho_1 + \rho_2 + \dots \\ &= \rho_0 + \sum_{j=1}^{\infty}\delta_j\rho_1^{(j)} + \sum_{j,k=1}^{\infty}\delta_j\delta_k\rho_2^{(j,k)} + \dots,\end{aligned} \tag{65}$$

where $\rho_m^{(j,\dots)}$ are assumed to be independent of δ_j. Inserting Eqs. (64) and (65) into (63), collecting terms of equal order in δ_j, and solving up to $\mathcal{O}[\delta_j^2]$ gives

$$\frac{1}{\Omega_0}\frac{d\rho_0}{dt} = i\left[\rho_0, \frac{\sigma_z}{2}\right], \tag{66}$$

$$\sum_{j=1}^{\infty}\frac{\delta_j}{\Omega_0}\frac{d\rho_1^{(j)}}{dt} = i\sum_{j=1}^{\infty}\delta_j\left\{\left[\rho_1^{(j)}, \frac{\sigma_z}{2}\right] + \left[\rho_0, \frac{\sigma_x}{2}\sin(\omega_j t + \varphi_j)\right]\right\}, \tag{67}$$

$$\sum_{j,k=1}^{\infty}\frac{\delta_j\delta_k}{\Omega_0}\frac{d\rho_2^{(j,k)}}{dt} = i\sum_{j,k=1}^{\infty}\delta_j\delta_k\left\{\left[\rho_2^{(j,k)}, \frac{\sigma_z}{2}\right] + \left[\rho_1^{(j)}, \frac{\sigma_x}{2}\sin(\omega_k t + \varphi_k)\right]\right\}. \tag{68}$$

For a Rabi driving experiment, in the frame of Eq. (59), we consider a qubit initialized to the north pole of the Bloch sphere. In the frame of Eq. (64), the corresponding initial state on the Bloch sphere is $\hat{x}$, or $\rho(0) = \frac{1}{2}(1+\sigma_x)$. Since ρ_0, $\rho_1^{(j)}$, and $\rho_2^{(j,k)}$ are independent of δ_j, the initial conditions for the different terms in the density operator expansion are given by $\rho_0(0) = \frac{1}{2}(1+\sigma_x)$, with $\rho_1(0) = \rho_2(0) = 0$.

Accounting for these initial conditions, it is possible to solve Eq. (67), independently, for each $\rho_1^{(j)}$ (results are given below). Making use of uniqueness theorems for Fourier transforms and differential equations, the resulting solution for ρ_1 is unique. Equation (67) can therefore be replaced by the decoupled equation

$$\frac{1}{\Omega_0}\frac{d\rho_1^{(j)}}{dt} = i\left[\rho_1^{(j)}, \frac{\sigma_z}{2}\right] + i\left[\rho_0, \frac{\sigma_x}{2}\sin(\omega_j t + \varphi_j)\right]. \tag{69}$$

In Eq. (68), we note the presence of mixed terms, involving parameters j and k. This is inconvenient; however, in the following derivations, we perform an average over the independent, fluctuating variables $\{\varphi_j, \varphi_k\} \in [0, 2\pi]$, which leads to a helpful simplification. Let us define the averaging procedure as

$$\langle f(\varphi)\rangle_\varphi = \frac{1}{2\pi}\int_0^{2\pi} f(\varphi)d\varphi. \tag{70}$$

In the derivations described below, it can be shown that

$$\left\langle\left[\rho_1^{(j)}, \frac{\sigma_x}{2}\sin(\omega_k t + \varphi_k)\right]\right\rangle_{\varphi_j,\varphi_k} = \delta_{jk}\left\langle\left[\rho_1^{(j)}, \frac{\sigma_x}{2}\sin(\omega_j t + \varphi_j)\right]\right\rangle_{\varphi_j}, \tag{71}$$

where δ_{jk} is the Kronecker δ-function. As a result, we find that $\langle\rho_2^{(j,k)}\rangle_{\varphi_j,\varphi_k} = \delta_{jk}\langle\rho_2^{(j,j)}\rangle_{\varphi_j} \equiv \delta_{jk}\langle\rho_2^{(j)}\rangle_{\varphi_j}$. Anticipating this step, we can preemptively eliminate the mixed terms in Eq. (68), so that the sum runs only over the variable j. As was the case for $\rho_1^{(j)}$, we can then independently solve for each $\rho_2^{(j)}$, obtaining a unique solution

for ρ_2. Equation (68) can therefore be replaced by the decoupled equation

$$\frac{1}{\Omega_0}\frac{d\rho_2^{(j)}}{dt} = i\left[\rho_2^{(j)}, \frac{\sigma_z}{2}\right] + i\left[\rho_1^{(j)}, \frac{\sigma_x}{2}\sin(\omega_j t + \varphi_j)\right]. \quad (72)$$

Thus, we may solve for the density matrix terms $\rho_1^{(j)}$ and $\rho_2^{(j)}$ independently, and combine the results for different j values afterwards.

Following the procedure described above, we perturbatively solve for ρ, apply initial conditions, and perform an average over the fluctuating variable φ_j, obtaining

$$\langle\rho(t)\rangle \approx \frac{1}{2} + \left[\frac{1}{2}\cos(\Omega_0 t) - \sum_{j=1}^{\infty}\delta_j^2 \frac{2\cos(\Omega_0 t) - 2\cos(\omega_j t) + (\Omega_0^2 - \omega_j^2)(t/\Omega_0)\sin(\Omega_0 t)}{8(\Omega_0^2 - \omega_j^2)^2/\Omega_0^4}\right]\sigma_x + \left[\frac{1}{2}\sin(\Omega_0 t) - \sum_{j=1}^{\infty}\delta_j^2 \frac{2\sin(\Omega_0 t) - 2(\omega_j/\Omega_0)\sin(\omega_j t) + (\Omega_0^2 - \omega_j^2)(t/\Omega_0)\cos(\Omega_0 t)}{8(\Omega_0^2 - \omega_j^2)^2/\Omega_0^4}\right]\sigma_y. \quad (73)$$

The perturbative expansion leading up to this result is formally related to a cumulant expansion [**?**], with an explicit, generalized averaging procedure.

In Eq. (73), we note that $\langle\rho\rangle$ diverges for noise occurring near the Rabi frequency, $\omega_j \approx \Omega_0$. Such unphysical behavior is also observed in the Rabi probability formula, $P_{0\to1}(t) = |V_{\rm ac}/\hbar\Omega|^2 \sin^2(\Omega t)$, when it is Taylor expanded with respect to the small parameter $V_{\rm ac}/\Delta \lesssim 1$. (Here, $\Omega = \sqrt{\Delta^2 + (V_{\rm ac}/\hbar)^2}$ is the Rabi frequency and Δ is the detuning.) In the derivation leading to Eq. (73), we have employed a similar Taylor expansion with respect to the small parameter $\delta_j = 2\pi\delta\nu_j/\Omega_0 \lesssim 1$, obtaining a similar divergence. Further away from $\omega_j = \Omega_0$, we expect Eq. (73) to be quite accurate. It is important to be aware of the singular behavior in Eq. (73), as it could affect some applications of this theory. However, in the remainder of this work, we focus our attention on quantum gate errors caused by laser noise. Since the singularity in Eq. (73) does not appear in such calculations, we simply ignore it from here on.

C. One-Photon Gate Fidelity

We now use Eq. (73) to compute quantum gate errors incurred during Rabi oscillations. We specifically consider gates defined by gate periods $t = 2\pi N/\Omega_0$ with $N = 1/2, 1, 3/2, \ldots$, where $N = 1/2$ corresponds to a π rotation, $N = 1$ corresponds to a 2π rotation, and so on. In the absence of fluctuations ($\delta_j = 0$), the ideal solution for such gates is given by

$$\rho_{\rm ideal}(N) = \frac{1}{2} + \frac{1}{2}(-1)^{2N}\sigma_x. \quad (74)$$

Defining the gate errors as $1 - F$, where $F = {\rm tr}[\langle\rho\rangle\rho_{\rm ideal}]$ is the gate fidelity, and making the substitutions $\omega_j \to 2\pi f$, $\Delta f \to df$, and

$$\sum_{j=1}^{\infty}\delta_j^2 \to \int_0^{\infty}\left(\frac{4\pi}{\Omega_0}\right)^2 S_{\delta\nu}(f)df, \quad (75)$$

we obtain

$${\rm error} = (2\pi\Omega_0)^2 \times \int_0^{\infty} S_{\delta\nu}(f)\frac{1 - (-1)^{2N}\cos(4\pi^2 N f/\Omega_0)}{(\Omega_0^2 - 4\pi^2 f^2)^2}df. \quad (76)$$

As noted above, this expression remains finite for all f, including $2\pi f = \Omega_0$.

Equation (76) is our main result, which may now be applied to cases of interest, including white noise and servo bumps. For the $t = 2\pi N/\Omega_0$ gates, defined above, with white noise defined in Eq. (32), we obtain the simple result

$${\rm error} = \frac{\pi^3 h_0 N}{\Omega_0} \qquad \text{(white noise)}. \quad (77)$$

For servo bumps, the frequency noise is defined in Eq. (39). To simplify the error calculation, we make use of the fact that the peak in $S_{\delta\nu}(f)$ is typically sharper and narrower than other frequency-dependent terms in Eq. (76). This sharp peak can be observed, for example, in Fig. 3(c). We therefore make the following substitution in Eq (76):

$$S_{\delta\nu}(f) \to \frac{s_g f_g^2}{2}\delta(f - f_g), \quad (78)$$

which yields the following expression for the gate error:

$${\rm error} \approx 2s_g(\pi f_g\Omega_0)^2\frac{1 - (-1)^{2N}\cos(4\pi^2 N f_g/\Omega_0)}{(\Omega_0^2 - 4\pi^2 f_g^2)^2} \qquad \text{(servo bump)}. \quad (79)$$

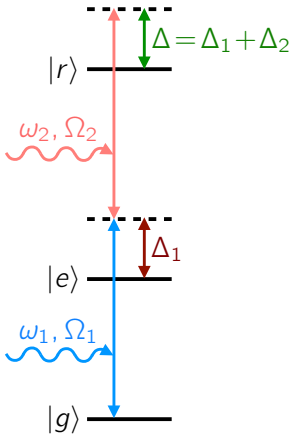

FIG. 4. Coupling scheme for two-photon Rabi oscillations in a ladder configuration, for states $|g\rangle$, $|e\rangle$, and $|r\rangle$. Two lasers are employed, with photon angular frequencies $\omega_{1,2}$ and associated Rabi angular frequencies $\Omega_{1,2}$. The lasers are detuned away from ladder excitations by angular frequencies Δ_1 and Δ_2.

As shown in later sections, the largest errors due to servo bumps occur when $\omega_g \approx 2\pi f_g = \Omega_0$. Evaluating Eq. (76) in this worst-case scenario gives

$$\text{error} \approx \frac{s_g(\pi N)^2}{4}. \tag{80}$$

D. Two-Photon Gate Fidelity

We can extend the time-series master equation approach to describe two-photon Rabi oscillations, for the excitation scheme shown in Fig. 4. We consider a three-level system $\{|g\rangle, |e\rangle, |r\rangle\}$ with level energies given by E_g, E_e, and E_r. We also consider two monochromatic lasers with angular frequencies ω_1 and ω_2 and Rabi angular frequencies Ω_1 and Ω_2. As before, we allow for phase fluctuations in both lasers, characterized by their individual noise spectral densities, $S_{1,\delta\nu}(f)$ and $S_{2,\delta\nu}(f)$:

$$\phi_i(t) = -\sum_{j=1}^{N} \delta\nu_{i,j} \cos(2\pi f_j t + \varphi_{i,j}), \tag{81}$$

where

$$\delta\nu_{i,j} = -2\sqrt{S_{i,\delta\nu}(f_j)\Delta f}. \tag{82}$$

Here, the random phases $\{\varphi_{i,j}\}$ are assumed to be independent for all i and j.

In analogy with Eq. (59), the full system Hamiltonian in the laboratory frame is now given by

$$\begin{aligned} H = {} & E_g|g\rangle\langle g| + E_e|e\rangle\langle e| + E_r|r\rangle\langle r| \\ & + \hbar\Omega_1 \cos(\omega_1 t)\left(e^{-i\phi_1}|e\rangle\langle g| + e^{i\phi_1}|g\rangle\langle e|\right) \\ & + \hbar\Omega_2 \cos(\omega_2 t)\left(e^{-i\phi_2}|r\rangle\langle e| + e^{i\phi_2}|e\rangle\langle r|\right) \end{aligned} \tag{83}$$

Moving to the rotating frame defined by

$$\begin{aligned} U(t) = \exp\Bigg[& i\left(\frac{2\omega_1 t}{3} + \frac{\omega_2 t}{3}\right)(|e\rangle\langle e| - |g\rangle\langle g|) \\ & + i\left(\frac{\omega_1 t}{3} + \frac{2\omega_2 t}{3}\right)(|r\rangle\langle r| - |e\rangle\langle e|)\Bigg] \end{aligned} \tag{84}$$

and applying an RWA, we obtain

$$\begin{aligned} H' \approx {} & \frac{\hbar\Delta}{2}|g\rangle\langle g| - \frac{\hbar\delta}{2}|e\rangle\langle e| - \frac{\hbar\Delta}{2}|r\rangle\langle r| \\ & + \frac{\hbar\Omega_1}{2}\left(e^{-i\phi_1}|e\rangle\langle g| + e^{i\phi_1}|g\rangle\langle e|\right) \\ & + \frac{\hbar\Omega_2}{2}\left(e^{-i\phi_2}|r\rangle\langle e| + e^{i\phi_2}|e\rangle\langle r|\right), \end{aligned} \tag{85}$$

where we have removed a constant energy term and defined $\hbar\Delta_1 = \hbar\omega_1 + E_g - E_e$, $\hbar\Delta_2 = \hbar\omega_2 + E_e - E_r$, $\Delta = \Delta_1 + \Delta_2$, as illustrated in Fig. 4, with $\delta = \Delta_1 - \Delta_2$.

As in the previous section, we next move to a fluctuation frame, defined by the transformation

$$\begin{aligned} U_\phi(t) = {} & e^{-i\phi_1/2 - i\phi_2/2}|g\rangle\langle g| \\ & + e^{i\phi_1/2 - i\phi_2/2}|e\rangle\langle e| + e^{i\phi_1/2 + i\phi_2/2}|r\rangle\langle r|, \end{aligned} \tag{86}$$

yielding the Hamiltonian

$$\begin{aligned} H'' \approx {} & \frac{\hbar}{2}\left(\Delta + \dot\phi_1 + \dot\phi_2\right)|g\rangle\langle g| \\ & + \frac{\hbar}{2}\left(-\delta - \dot\phi_1 + \dot\phi_2\right)|e\rangle\langle e| + \frac{\hbar}{2}\left(-\Delta - \dot\phi_1 - \dot\phi_2\right)|r\rangle\langle r| \\ & + \frac{\hbar\Omega_1}{2}(|e\rangle\langle g| + |g\rangle\langle e|) + \frac{\hbar\Omega_2}{2}(|r\rangle\langle e| + |e\rangle\langle r|). \end{aligned} \tag{87}$$

Now if we assume that $|\delta| \gg \Omega_1, \Omega_2, |\dot\phi_1|, |\dot\phi_2|$, and that the system wavefunction $|\psi\rangle$ is not initialized into state $|e\rangle$, then at later times we still have $|\langle\psi|e\rangle|^2 \ll 1$. Hence, it is a good approximation to slave $|e\rangle$ to states $|g\rangle$ and $|r\rangle$, such that

$$|e\rangle \approx \frac{\Omega_1}{\delta}|g\rangle + \frac{\Omega_2}{\delta}|r\rangle. \tag{88}$$

Eliminating $|e\rangle$ from H'', we arrive at an effective 2D Hamiltonian describing the dynamical evolution of $|g\rangle$ and $|r\rangle$:

$$H_{2D} \approx \frac{\hbar\tilde\Omega_0}{2}\sigma_x - \frac{\hbar}{2}\left(\Delta_+ + \dot\phi_1 + \dot\phi_2\right)\sigma_z, \tag{89}$$

where we define $\Delta_+ = \Delta + (\Omega_1^2 - \Omega_2^2)/2\delta$, $\tilde\Omega_0 = \Omega_1\Omega_2/\delta$, $\sigma_z = |r\rangle\langle r| - |g\rangle\langle g|$, and $\sigma_x = |r\rangle\langle g| + |g\rangle\langle r|$, and we have again removed a constant energy term.

In the absence of noise ($\dot\phi_1, \dot\phi_2 = 0$), H_{2D} describes rotations tilted slightly away from the x axis, which is undesirable from a gating perspective. This situation can be avoided by adopting the special detuning value defined by the relation $\Delta_+ = 0$, or equivalently,

$$\Delta = \Delta_1\left(1 - \sqrt{1 + \frac{\Omega_1^2 - \Omega_2^2}{2\Delta_1^2}}\right). \tag{90}$$

For this case, we obtain

$$H_{2D} \approx \frac{\hbar\tilde{\Omega}_0}{2}\sigma_x - \frac{\hbar}{2}\left(\dot{\phi}_1 + \dot{\phi}_2\right)\sigma_z, \tag{91}$$

which maps immediately onto Eq. (61) of our previous one-photon analysis.

In the one-photon calculation, we were able to make progress by noting that the random phases φ_j, corresponding to frequency variables ω_j, were independent, yielding additive contributions to the total error in the quantum gates. Now in the two-photon case, the random variables φ_{j1} and φ_{j2}, corresponding to lasers 1 and 2, are also independent; therefore, their contributions to the total error should also be additive. Accounting for the separate power spectral densities in the two lasers, we obtain the following two-photon results, for gates defined by $t = 2\pi N/\tilde{\Omega}_0$, with $N = 1/2, 1, 3/2, \ldots$. For the white noise defined by the parameters h_1 and h_2 in the two lasers, we obtain

$$\text{error} = \frac{\pi^3(h_1 + h_2)N}{\tilde{\Omega}_0} \qquad \text{(white noise)}. \tag{92}$$

For the servo-bump model of laser phase noise, the differences in the lasers are characterized by the total power in the separate servo bumps (s_{g1} and s_{g2}) and their corresponding peak frequencies (f_{g1} and f_{g2}). The resulting error for two-photon gates is given by

$$\text{error} \approx 2s_{g1}(\pi f_{g1}\tilde{\Omega}_0)^2 \frac{1-(-1)^{2N}\cos(4\pi^2 N f_{g1}/\tilde{\Omega}_0)}{(\tilde{\Omega}_0^2 - 4\pi^2 f_{g1}^2)^2} + 2s_{g2}(\pi f_{g2}\tilde{\Omega}_0)^2 \frac{1-(-1)^{2N}\cos(4\pi^2 N f_{g2}/\tilde{\Omega}_0)}{(\tilde{\Omega}_0^2 - 4\pi^2 f_{g2}^2)^2} \qquad \text{(servo bump)}. \tag{93}$$

V. DYNAMICAL SIMULATIONS OF RABI GATES WITH PHASE NOISE

In this section, we perform simulations of Rabi oscillations, including laser phase fluctuations. We specifically consider the effects of white noise, defined in Eq. (32), for a range of noise amplitudes, $h_0 \in (0, 4000)$ Hz^2/Hz. We also consider servo bumps, defined in Eq. (39), for fixed parameter values of $h_g = 1100$ Hz^2/Hz and $\sigma_g = 1.4$ kHz, which are similar to the experimental values obtained in Sec. III. Since gate errors caused by servo bumps are maximized when the bump peak occurs near the Rabi frequency, $f_g \approx (\Omega_0/2\pi)$, we focus on the parameter range $f_g \in (0, 2) \times (\Omega_0/2\pi)$. In the latter simulations, we set the white-noise amplitude to $h_0 = 0$, to focus exclusively on the servo bump. For all simulations, we adopt the typical Rabi frequency $\Omega_0 = 1 \times 2\pi$ MHz. For the two-photon gates, for simplicity, we assume that both lasers have the same noise spectra.

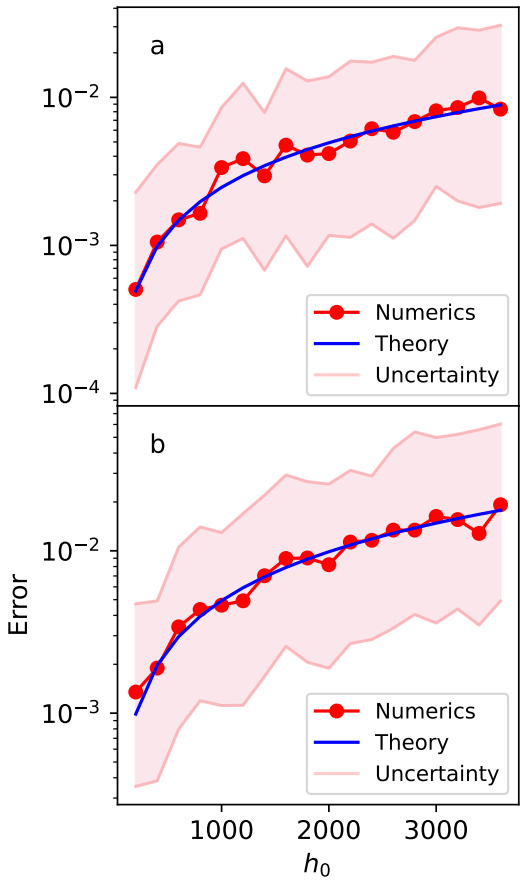

FIG. 5. Rabi errors for one-photon Rabi oscillations due to white phase noise, plotted as a function of noise amplitude h_0. Results are obtained following the procedure described in Sec. V A for (a) π rotations and (b) 2π rotations. Red markers represent averages from numerical simulations, while pink shading shows the corresponding 1σ error bars.Blue curves show theoretical results from Eq. (77).

A. One-photon gates

We first consider one-photon Rabi gates with laser phase noise. The gates are defined in Sec. IV C, with $N = 1/2$ (π rotations) and $N = 1$ (2π rotations). As previously, we assume that the qubit is driven resonantly. Defining $|\psi(t)\rangle = c_g(t)|g\rangle + c_e(t)|e\rangle$, the Schrödinger equation associated with Eq. (60) can be written as

$$\dot{c}_g = -i\frac{\Omega_0}{2}e^{-i\phi(t)}c_e, \tag{94}$$

$$\dot{c}_e = -i\frac{\Omega_0}{2}e^{i\phi(t)}c_g. \tag{95}$$

To solve these equations, we first obtain a random time trace for $\phi(t)$ from Eq. (56). The infinite series expansion must be truncated and we therefore write

$$\phi(t_k) = \sum_{j=1}^{M/2}\sqrt{2S_\phi^{\text{1-sided}}(f_j)\Delta f}\cos(2\pi f_j t_k + \varphi_j), \tag{96}$$

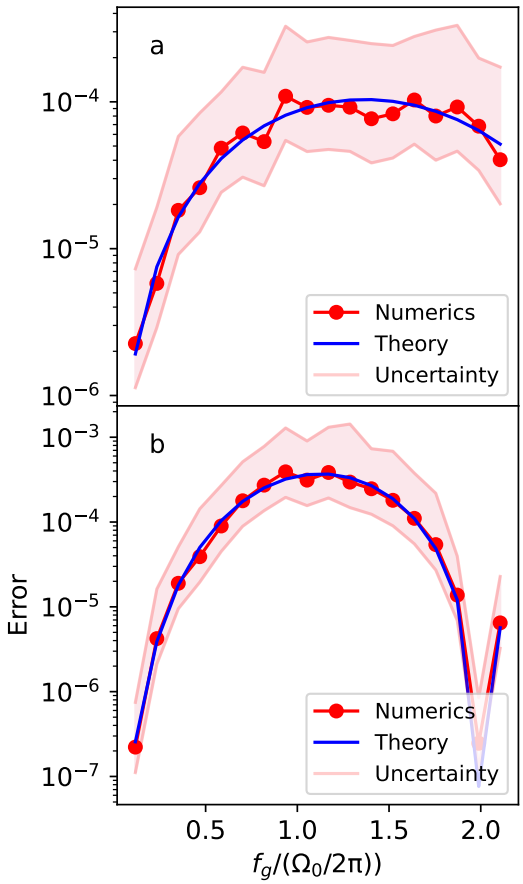

FIG. 6. Rabi errors for one-photon Rabi oscillations due to servo-bump phase noise. Results are plotted as a function of the center frequency of the servo bump f_g, scaled by the Rabi frequency $\Omega_0/2\pi = 1$ MHz, with additional noise parameters described in Sec. V A. Similar to Fig. 5, (a) shows results for π rotations and (b) shows results for 2π rotations. Theory results are obtained from Eq. (79).

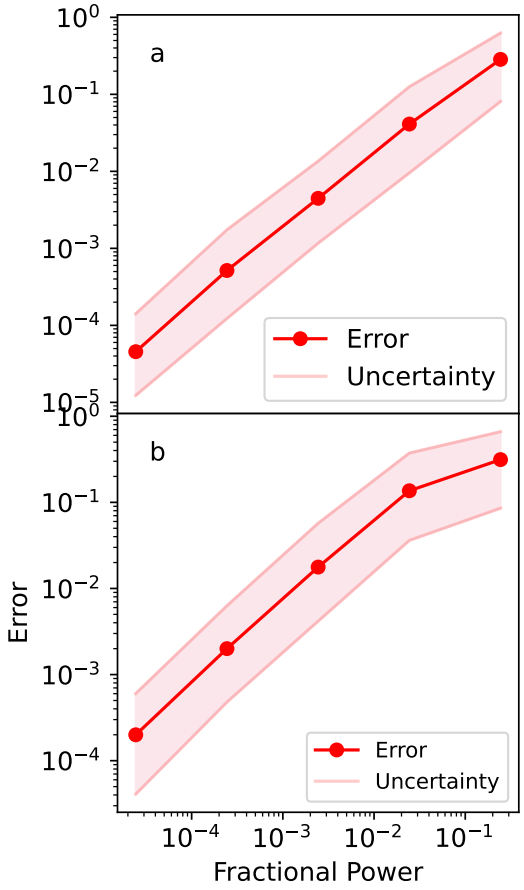

FIG. 7. Rabi errors for one-photon Rabi oscillations due to servo-bump phase noise: (a) π rotations, (b) 2π rotations. Calculations are very similar to Fig. 6, except that here, the central peak frequency of the servo bump is held fixed, while the total power s_g is varied, where s_g is defined in Eq. (41).

where $\Delta f = f_{j+1} - f_j = 1/T$ for times sampled in the range $0 \leq t_k \leq T$, with $t_{k+1} - t_k = T/M$, according to the Nyquist sampling theorem. For the simulations described below, white noise poses the most serious challenge to numerical convergence. In this case, we find that a frequency bandwidth of $f_{M/2} = 10$ MHz is sufficient for our purposes, and that convergence is achieved when $M \approx 10^3$. Equations (94) and (95) are then solved numerically, using the computed time series. Statistical properties are obtained by performing averages over results from many random time series. As in previous sections, the resulting gate errors are defined as $1 - F$, where $F = \mathrm{tr}[\langle\rho\rangle\rho_{\mathrm{ideal}}]$.

In Fig. 5, we plot gate errors for π and 2π rotations in the presence of white noise. In this figure, as in all figures that follow, the numerical averages are shown as red markers, while 1σ error bars are shown with pink shading. Theoretical results are shown as blue curves, obtained from Eq. (77). For typical white-noise amplitudes ($h_0 < 100$ Hz^2/Hz), the observed error levels are low. Theoretical results are found to reproduce the numerical ones quite accurately.

In Fig. 6, we plot π and 2π gate errors for Rabi oscillations in the presence of servo-bump noise. Here the results are plotted as a function of the center frequency of the servo bump, scaled by the Rabi frequency $\Omega_0/2\pi = 1$ MHz. Corresponding theory results are also shown, based on Eq. (79). Again, the theoretical results are found to describe well the non-monotonic behavior of the numerical results. As expected, gate errors are maximized for servo bumps centered near the Rabi frequency. As anticipated from the theoretical calculations of Sec. IV B, gate errors are strongly suppressed for the condition $f_g = 2(\Omega_0/2\pi)$. This is an interesting interference effect induced by the shape of Gaussian noise peaks, which isn't observed, for example, in the case of white noise. Such error suppression could potentially be leveraged for reducing Rabi gate errors.

In Fig. 7, we also show results for servo-bump noise. In this case, the center frequency of the servo bump is held

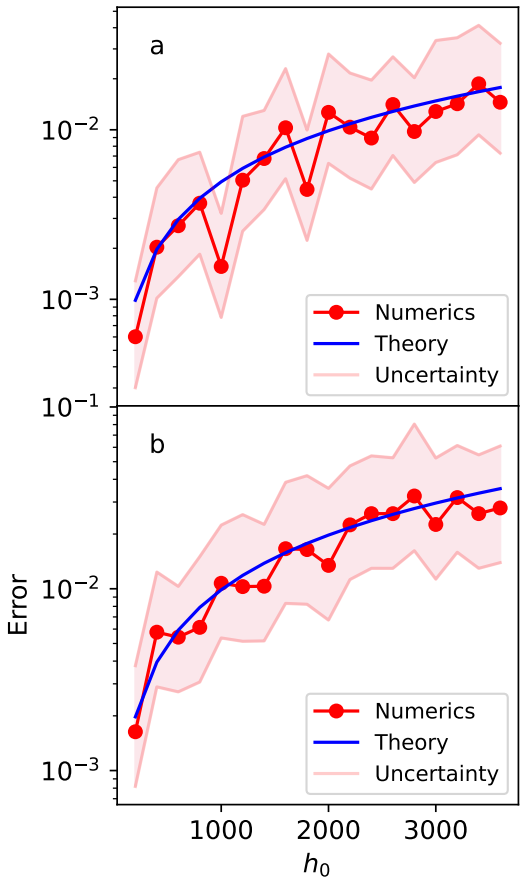

FIG. 8. Rabi errors for two-photon Rabi oscillations due to white phase noise: (a) π rotations, (b) 2π rotations. All simulations and plots are analogous to Fig. 5, while theory results are given by Eq. (92).

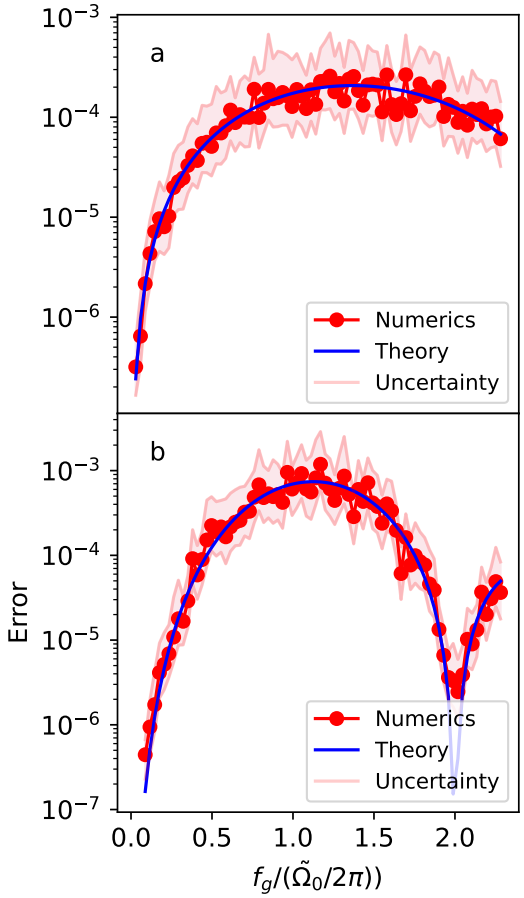

FIG. 9. Rabi errors for for two-photon Rabi oscillations due to servo-bump phase noise: (a) π rotations, (b) 2π rotations. All simulations and plots are analogous to Fig. 6, while theory results are given by Eq. (93).

fixed at the experimentally observed value $f_g = 234$ kHz reported in Sec. III, while the total noise power in the servo bump is varied, using the definition of s_g in Eq. (41).Plotted on a log-log scale, we observe an initial linear dependence of gate error on noise power.

B. Two-photon gates

Two-photon gates are described in Sec. IV D. For the gates considered here, both lasers are detuned, in contrast with the one-photon gates described above. Defining $|\psi(t)\rangle = c_g(t)e^{-i\Delta t/2}|g\rangle + c_e(t)e^{i\delta t/2}|e\rangle + c_r(t)e^{i\Delta t/2}|r\rangle$, the Schrödinger equation associated with Eq. (85) can be written as

$$\dot{c}_g = -i\frac{\Omega_1}{2}e^{i\phi_1(t)}e^{i\Delta_1 t}c_e, \tag{97}$$

$$\dot{c}_e = -i\frac{\Omega_1}{2}e^{-i\phi_1(t)}e^{-i\Delta_1 t}c_g - i\frac{\Omega_2}{2}e^{i\phi_2(t)}e^{i\Delta_2 t}c_r, \tag{98}$$

$$\dot{c}_r = -i\frac{\Omega_2}{2}e^{-i\phi_2(t)}e^{-i\Delta_2 t}c_e. \tag{99}$$

As in experiments, the detuning parameters in two-photon simulations should be chosen carefully. Referring to the notation of Sec. IV D, we adopt the following criteria: (1) the effective, two-photon Rabi frequency is chosen to be $\tilde{\Omega}_0 = \Omega_1\Omega_2/\delta = 1 \times 2\pi$ MHz (as in the one-photon simulations), (2) the ratio $\delta/\tilde{\Omega}_0$ should be large enough to avoid populating the intermediate level $|e\rangle$, but small enough for simulations to complete in a reasonable time (here we choose $\delta/\tilde{\Omega}_0 = 100$). For convenience, we also choose $\Omega_1 = \Omega_2$, and we note that the resonance condition, Eq. (90), must be satisfied. These combined criteria yield $\Delta_1 = -\Delta_2 = 5 \times 2\pi$ GHz, $\Omega_1 = \Omega_2 = 100 \times 2\pi$ MHz, and $\delta = 10 \times 2\pi$ MHz. These choices yield a resonant excitation of the state $|r\rangle$ ($\Delta = 0$; see Fig. 4), consistent with our resonant excitation scheme for one-photon gates. For convenience, we assume identical noise parameters for the two lasers (e.g., $h_1 = h_2$, etc.), although the time series for $\phi_1(t)$ and $\phi_2(t)$ are still generated independently from Eq. (96). Finally, Eqs. (97)-(99) are solved numerically for many random time series, and averaged.

Figure 8 shows two-photon results for the case of white phase noise. The corresponding theoretical results are given in Eq. (92). These results may be compared directly to one-photon gates. Indeed, the two-photon gate errors appear similar in shape, but doubled in magnitude, as compared to Fig. 5. This is consistent with the expectation that errors should be additive in the limit of weak noise, as confirmed in Sec. IV D.

Figure 9 shows two-photon results for the case of servo-bump phase noise. Here, the theoretical results are given in Eq. (93). Again, we observe an approximate doubling of the gates errors as compared to the single-photon case, shown in Fig 6. In all cases, the theoretical results of Sec. IV appear quite accurate.

VI. BANDWIDTH-LIMITED PHASE NOISE AND THE QUASISTATIC LIMIT

Narrow bandwidth noise may provide a good approximation for certain highly filtered lasers. In this section, we extend the previous theoretical approach to the case of quasistatic phase noise, where the spectral content of the noise is restricted to very low frequencies. To begin, we consider the more general situation of bandwidth-limited white noise, defined as

$$S_{\delta\nu}(f) = \begin{cases} h_0 & \text{when} \quad |f| \le f_c, \\ 0 & \text{when} \quad |f| > f_c. \end{cases} \tag{100}$$

A noise spectrum of this type could describe a strongly filtered laser with no noise except a broadened carrier signal.

Di Domenico et al. [12] have studied how band-limited white noise is manifested in laser field noise, $S_E(f)$. They observe two distinct behaviors, with an abrupt transition between them occurring at $f_c = \pi^2 h_0/8\ln(2) \approx 1.78 h_0$. When $f_c \gtrsim 1.78 h_0$, $S_E(f)$ takes the form appropriate for white noise, which we previously characterized in Sec. II C. When $f_c \lesssim 1.78 h_0$, Eqs. (13) and (27) are readily solved, yielding

$$S_E(f) \approx \frac{|E_0|^2}{\sqrt{16\pi h_0 f_c}} e^{-f^2/4h_0 f_c}, \tag{101}$$

$$S_i(f) \approx \sqrt{\frac{3}{16\pi^3 h_0 t_d^2 f_c^3}}\, e^{-3f^2/16\pi^2 h_0 t_d^2 f_c^3}. \tag{102}$$

In the context of Rabi gate operations, when we also have $f_c \ll \Omega_0/2\pi$, we refer to this compressed-noise regime as quasistatic.

The singular nature of quasistatic noise causes the interrelations between $S_\phi(f)$, $S_E(f)$, and $S_i(f)$, embodied in Eqs. ((28) and (29), to collapse. This is particularly evident in Eq. (102) which does not exhibit the scallop features, typical of self-heterodyne measurements. We also note that the FWHM of the broadened carrier signals in Eqs. (101) and (102) are no longer related and exhibit distinct scaling properties. Hence, $S_i(f)$ may no longer be taken as a proxy for $S_E(f)$.

A. Master Equation Approach

While $S_{\delta\nu}(f), S_E(f)$, and $S_i(f)$ depend only on h_0 and f_c, Rabi gate errors also depend on Ω_0. Single-photon gate errors caused by finite-bandwidth white noise can be computed from Eq. (76), without approximation, giving

$$\begin{aligned} \text{error} = \frac{\pi h_0}{2\Omega_0}\Bigg\{ & \frac{2y[1-(-1)^{2N}\cos(2\pi N y)]}{1-y^2} \\ & + 2\,\text{Arctanh}(y) + \text{Ci}[2\pi N(1-y)] - \text{Ci}[2\pi N(1+y)] \\ & - 2\pi N\,\text{Si}[2\pi N(1-y)] + 2\pi N\,\text{Si}[2\pi N(1+y)]\Bigg\}, \end{aligned} \tag{103}$$

where $\text{Ci}(x)$ and $\text{Si}(x)$ are cosine and sine integral functions [15], and $y \equiv 2\pi f_c/\Omega_0$.

In the limit $f_c \gg \Omega_0$, we can use Eq. (103) to recover the gate-error results obtained in Eqs. (77) and (92) for ordinary white noise. In the opposite limit, $f_c \lesssim \Omega_0$, we note that the weak-noise approximation used to derive Eq. (103) also requires that $\sqrt{h_0 f_c} \lesssim \Omega_0$, and therefore $h_0, f_c \lesssim \Omega_0$. In this regime, we obtain the following results for $2\pi N$ Rabi gates:

$$\text{error} \approx \begin{cases} \frac{8\pi^2 h_0 f_c}{\Omega_0^2} & (N = 1/2, 3/2, 5/2, \dots), \\ \frac{32\pi^6 h_0 f_c^3 N^2}{3\Omega_0^4} & (N = 1, 2, 3, \dots). \end{cases} \tag{104}$$

Here we note that the results do not depend on f_c being larger or smaller than h_0. As in Sec. IV D, the two-photon gate errors are additive, giving

$$\text{error} = \begin{cases} \frac{8\pi^2 (h_1 f_{c1} + h_2 f_{c2})}{\Omega_0^2} & (N = 1/2, 3/2, 5/2, \dots), \\ \frac{32\pi^6 (h_1 f_{c1}^3 + h_2 f_{c2}^3) N^2}{3\Omega_0^4} & (N = 1, 2, 3, \dots). \end{cases} \tag{105}$$

Qualitatively different types of behavior are observed in Eqs. (103)-(105) for half vs. full rotations, which can be understood as follows. In the quasistatic limit, frequency noise causes the Rabi rotation axis to shift away from the equator of the Bloch sphere, naturally inducing gate errors. We have performed numerical simulations of half (i.e., π) rotations for such band-limited noise, finding very good agreement with Eqs. (103)-(105). For the special case of full rotations, however, the Bloch state returns to its initial value (to leading order in a noise expansion). A secondary effect of the frequency noise is to increase the rotation speed, yielding an over-rotation or under-rotation. However this latter effect is higher-order, resulting in smaller errors for full rotations. In other words, for the special case of full rotations, in the extreme limit of quasistatic noise, the leading order contribution to gate error vanishes; for all other cases, lower-order contributions are present.

We plot Eq. (103) in Fig. 10, along with results of numerical simulations of 2π rotations, for bandwidth-limited white noise. It is evident that our theory captures the majority of the errors arising from such noise spectra.

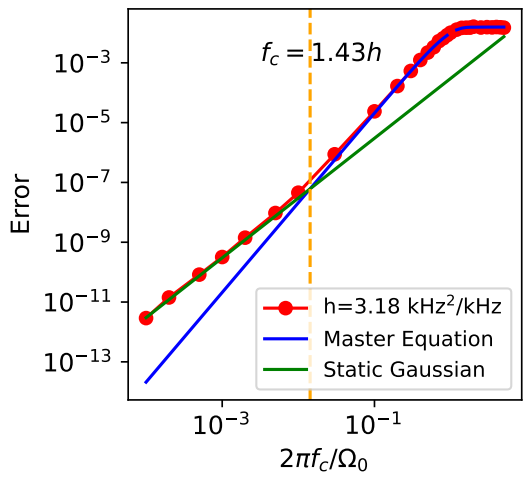

FIG. 10. Rabi errors for one-photon 2π rotations, due to band-limited white frequency noise with fixed amplitude $h_0 = 3.18$ kHz^2/kHz, as a function of the noise bandwidth. Red data are obtained from numerical simulations, while the blue curve is Eq. (103) and the green curve is Eq. (110). The vertical dashed line corresponds to the crossover criterion, $f_c \approx 1.43h_0$.

However, the theory breaks down in the limit of small f_c/h_0. Specifically, we find that Eq. (103) fails when $f_c \lesssim 1.43h_0$. (Failure also requires that $f_c \lesssim \Omega_0/2\pi$.) We attribute this failure to the fact that the Master equation derivation in Sec. IV employs an expansion in powers of the noise strength, retaining only the leading-order term. Hence, for the special case of full rotations, in the quasistatic limit, where the leading-order contribution to the gate error vanishes, our theory does not capture the central physics.

B. Quasistatic Gaussian-Distributed Noise

To obtain an accurate solution for the singular problem of full rotations in the quasistatic limit, we modify the Master equation approach of Sec. IV B. The starting point for these calculations is the fluctuating frame Hamiltonian of Eq. (62),

$$H = \frac{\hbar\Omega_0}{2}\sigma_z + \frac{h\delta\nu}{2}\sigma_x, \tag{106}$$

which describes a rotation tilted slightly away from the desired Rabi rotation axis. In the quasistatic limit, the frequency fluctuation $\delta\nu$ remains constant for the duration of the gate operation.

The dynamics of the density matrix is readily solved for a static Hamiltonian, yielding

$$\begin{aligned}\rho(t) = \frac{1}{2} &+ \left\{\frac{(2\pi\delta\nu)^2}{2{\Omega_0'}^2} + \frac{\Omega_0^2}{2{\Omega_0'}^2}\cos(\Omega_0' t)\right\}\sigma_x \\ &+ \left\{\frac{\Omega_0}{2\Omega_0'}\sin(\Omega_0' t)\right\}\sigma_y \\ &+ \left\{\frac{2\pi\delta\nu\,\Omega_0}{2{\Omega_0'}^2}\left[1-\cos(\Omega_0' t)\right]\right\}\sigma_z,\end{aligned} \tag{107}$$

where $\Omega_0' \equiv \sqrt{\Omega_0^2 + (2\pi\delta\nu)^2}$, and we have adopted the same initial conditions as in Sec. IV B, namely, $\rho(0) = \frac{1}{2}(1+\sigma_x)$.

Equation (107) describes the evolution of a pure state in a rotating frame. We now assume the fluctuation $\delta\nu$ is drawn from a Gaussian distribution with probability distribution

$$p_{\delta\nu} = \frac{1}{\sigma_{\delta\nu}\sqrt{2\pi}} e^{-(\delta\nu)^2/2\sigma_{\delta\nu}^2}. \tag{108}$$

Here, the connection to the bandwidth-limited white-noise power spectrum in Eq. (100) is provided through the variance:

$$\sigma_{\delta\nu}^2 = \langle(\delta\nu)^2\rangle_{\delta\nu} = \int_{-\infty}^{\infty} S_{\delta\nu}(f)df = 2h_0 f_c. \tag{109}$$

As in Sec. IV C, the error in a Rabi gate defined by the gate period $t = 2\pi N/\Omega_0$ is given by error $= 1 - \mathrm{tr}[\langle\rho\rangle_{\delta\nu}\rho_{\mathrm{ideal}}]$, where ρ_{ideal} is defined in Eq. (74). Expanding Eq. (107) in leading powers of $2\pi\delta\nu/\Omega_0$, we obtain the following result for one-photon quasistatic gate errors:

$$\text{error} \approx \begin{cases} \frac{8\pi^2 h_0 f_c}{\Omega_0^2} & (N = 1/2, 3/2, 5/2, \dots), \\ \frac{48\pi^6 h_0^2 f_c^2 N^2}{\Omega_0^4} & (N = 1, 2, 3, \dots). \end{cases} \tag{110}$$

For the case of half-rotations ($N = 1/2, 3/2, 5/2, \dots$), we note that Eq. (110) agrees with Eq. (104). However, for full rotations ($N = 1, 2, 3, \dots$), the results disagree. We plot Eq. (110) as a green line in Fig. 10, finding that it accurately captures the physics of full-rotations in the quasistatic regime.

Turning to two-photon gates, we follow a similar procedure. The Hamiltonian in the fluctuating frame, Eq. (91), can be rewritten as

$$H = \frac{\hbar\tilde{\Omega}_0}{2}\sigma_z + \frac{h(\delta\nu_1 + \delta\nu_2)}{2}\sigma_x, \tag{111}$$

where $\delta\nu_1$ and $\delta\nu_2$ are the fluctuations of the two different lasers. The problem is identical to Eq. (106), after making the replacements $\Omega_0 \to \tilde{\Omega}_0 = \Omega_1\Omega_2/\delta$ and $\delta\nu \to \delta\nu_1 + \delta\nu_2$. We assume independent Gaussian distributions for $\delta\nu_1$ and $\delta\nu_2$, as defined by their separate variances, $\sigma_{\delta\nu_1}^2 = 2h_1 f_{c1}$ and $\sigma_{\delta\nu_2}^2 = 2h_2 f_{c2}$. The error

calculation then gives

$$\text{error} \approx \begin{cases} \frac{8\pi^2(h_1 f_{c1}+h_2 f_{c2})}{\bar{\Omega}_0^2} & (N = 1/2, 3/2, 5/2, \dots), \\ \frac{48\pi^6(h_1 f_{c1}+h_2 f_{c2})^2 N^2}{\bar{\Omega}_0^4} & (N = 1, 2, 3, \dots). \end{cases} \tag{112}$$

VII. INTENSITY NOISE

Time dependent intensity fluctuations are written as

$$I(t) = I_0 + \delta I(t) = I_0[1 + \alpha_I(t)] \tag{113}$$

where I_0 is the intensity of the noise-free laser and $\alpha_I(t)$ is the time-varying relative intensity fluctuation. The time varying Rabi frequency due to intensity noise for a one-photon process is

$$\Omega(t) = \Omega_0\sqrt{1 + \alpha_I(t)} \tag{114}$$

where Ω_0 is the constant Rabi frequency.

The relative intensity noise (RIN) is the root-mean-square(RMS) value of the relative intensity fluctuations. In the following we will assume that $\alpha_I(t)$ is wide-sense stationary, so that the RIN level is independent of time. The RIN level can be written in terms of the power spectrum of relative intensity noise as

$$\text{RIN} = \sqrt{\int_{-\infty}^{\infty} d\nu\, S_I(\nu)} \tag{115}$$

where

$$S_I(\nu) = \int_{-\infty}^{\infty} d\tau\, R_I(\tau) e^{-\imath 2\pi\nu\tau} \tag{116}$$

and $R_I(\tau)$ is the intensity auto-correlation function as defined in Eq. ().

In principle the effect of intensity noise on gate fidelity can be calculated using methods similar to those used in previous sections for laser phase noise. In certain types of lasers, including semiconductor diode lasers, relaxation oscillations may lead to intensity noise at frequencies of several GHz[]. In optically pumped solid state lasers relaxation oscillations tend to be limited to much lower, sub MHz frequencies. The analysis here is limited to the case of intensity noise spectra that are substantially less than the Rabi frequency, which enables us to use a simplified quasi-static description of the noise.

We could also use the quasi-static theory to evaluate the effect of near-DC intensity noise components. We will compare these two methods of studying intensity noise in Sec. **??** and Sec. **??**.

Assume that x follows normal distribution with zero mean and variance σ:

$$f(x) = \frac{1}{\sqrt{2\pi}\sigma} e^{-\frac{x^2}{2\sigma^2}} \tag{117}$$

Here σ is the root-mean-square(RMS) intensity noise, which is the RIN level that we measure in labs.

Under this situation, the Rabi frequency for a two level system is then:

$$\Omega = \Omega_0\sqrt{1 + x} \tag{118}$$

where Ω_0 is the Rabi frequency when the intensity noise does not exist. Here to make the expression valid we need $-1 \le x \le 1$, which means the intensity noise is not greater than the signal.

Under the setting that $-1 \le x \le 1$, we need to modify the distribution of x to be a truncated-Gaussian:

$$f(x) = \begin{cases} \frac{1}{\sqrt{2\pi}\sigma \mathbf{Erf}(\frac{1}{\sqrt{2}\sigma})} e^{-\frac{x^2}{2\sigma^2}}, & \text{if } -1 \le x \le 1 \\ 0, & \text{otherwise} \end{cases}$$

In resonant Rabi oscillation the population probability for the ground state $|g\rangle$ is:

$$P_g = \cos^2(\frac{\Omega t}{2}) \tag{119}$$

Suppose we are interested on the expectation value of P_e after N cycles driven by a laser with intensity noise, $t_N = N\frac{2\pi}{\Omega_0}$. Then the expected value of P_e can be calculated by the following integral:

$$\mathbb{E}[P_g] = \frac{1}{\sqrt{2\pi}\sigma \mathbf{Erf}(\frac{1}{\sqrt{2}\sigma})} \int_{-1}^{1} \cos^2(\frac{\Omega t_N}{2}) e^{-\frac{x^2}{2\sigma^2}} dx \tag{120}$$

$$= \frac{1}{\sqrt{2\pi}\sigma \mathbf{Erf}(\frac{1}{\sqrt{2}\sigma})} \int_{-1}^{1} \cos^2(N\pi\sqrt{1+x}) e^{-\frac{x^2}{2\sigma^2}} dx \tag{121}$$

By assuming that x is very small, and doing Talor expansion on the cosine part of the integral, we get the following approximation to second order:

$$\cos^2(N\pi\sqrt{1+x}) \approx 1 - \frac{N^2\pi^2 x^2}{4} \tag{122}$$

By plugging the approximation back and doing Gaussian integral on x between -1 and 1, we get:

$$\mathbb{E}[P_g] = 1 - \frac{N^2\pi^2\sigma^2}{4} + \frac{N^2\pi^{\frac{3}{2}}}{2\sqrt{2}} \frac{\sigma e^{-\frac{1}{2\sigma^2}}}{\mathbf{Erf}(\frac{1}{\sqrt{2}\sigma})} \tag{123}$$

The last term, with a $e^{-\frac{1}{2\sigma^2}}$ term, is zero in many orders of expansion. A good approximation will then be:

$$\mathbb{E}[P_g] = 1 - \frac{N^2\pi^2\sigma^2}{4} \tag{124}$$

To conclude, we can write the error predicted by quasi-static model to be:

$$\text{Error} = \frac{N^2\pi^2\sigma^2}{4} \tag{125}$$

For a certain RIN level σ, to make the oscillation amplitude decay by a factor of 1/e, we need the time $N_{1/e}$(in oscillation cycles) to be;

$$N_{1/e} = \frac{1.59}{\pi\sigma} \tag{126}$$

For two-photon Rabi oscillations ,When $\delta = \Delta_1 - \Delta_2 \gg |\Omega_1|, |\Omega_2|$, solving the Schrodinger equations gives the following approximate expression for the population on the Rydberg state $|r\rangle$, assuming initially $|c_g(0)|^2 = 1, |c_e(0)|^2 = |c_r(0)|^2 = 0$:

$$|c_r(t)|^2 = \sin^2(\frac{\Omega_0 t}{2}) \tag{127}$$

Here $v = \Omega_1\Omega_2/\delta$. This expression is also only true when $\Delta_+ = \Delta_1 + \Delta 2 + \frac{|\Omega_1|^2 - |\Omega_2|^2}{2\delta} = 0$ is satisfied. This condition guarantees a full population transfer between the ground state $|g\rangle$ and the Rydberg state$|r\rangle$.

When $\Delta_+ \neq 0$, expression (127) becomes:

$$|c_r(t)|^2 = \frac{\Omega_0^2}{\Omega'^2}\sin^2(\frac{\Omega' t}{2}) \tag{128}$$

where $\Omega'^2 = \tilde{\Omega}_0^2 + |\Delta_+|^2$.

In our following discussions, we always assueme that our noiseless system has $\Delta_+ = 0$.

If the two lasers driving the two-photon Rabi oscillations both have intensity noise:

$$\begin{aligned} I_1(t) &= I_{1_0} + \delta I_1(t) = I_{1_0}(1 + x_1(t)) \\ I_2(t) &= I_{2_0} + \delta I_2(t) = I_{2_0}(1 + x_2(t)) \end{aligned} \tag{129}$$

Assume that x_1 and x_2 both has normal distribution with 0 mean and variance σ_1^2 and σ_2^2:

$$f(x_i) = \frac{1}{\sqrt{2\pi}\sigma_i} e^{\frac{x_i^2}{2\sigma_i^2}} \tag{130}$$

where $i = 1, 2$.

Under this model, the modified Rabi rate Ω_i' will be:

$$\Omega_i' = \Omega_i\sqrt{1 + x_i}, i = 1, 2 \tag{131}$$

Set $t_N = N\frac{2\pi}{\Omega_0}$, then the expected value of Rydberg state population can be calculated with the following integral, under the condition that $\Delta_+ = 0$:

$$\begin{aligned} \mathbb{E}[P_r] = \frac{1}{2\pi\sigma_1\sigma 2}\int_{-\infty}^{\infty} dx_1 \\ \int_{-\infty}^{\infty} \sin^2(N\pi\sqrt{(1+x_1)(1+x_2)}) e^{\frac{x_1^2}{2\sigma_1^2}} e^{\frac{x_2^2}{2\sigma_2^2}} dx_2 \end{aligned} \tag{132}$$

Expanding the sin term in the integral to second order and evaluating the integral gives

an estimate for the expectation of the state occupanct occupancy, which is also the expected population error in Rabi oscillations

$$\mathbb{E}[P_r] = \frac{N^2\pi^2\sigma_1^2}{4} + \frac{N^2\pi^2\sigma_2^2}{4}. \tag{133}$$

VIII. SUMMARY AND DISCUSSION

In this paper, we theoretically investigated errors in quantum gate operations of neutral-atom qubits. We focused on a noise mechanism that dominates many qubit experiments: phase fluctuations of the driving laser. We considered both one and two-photon Rabi oscillations. We also considered generic noise spectra, such as flat-background (white) noise, and noise peaked at finite frequencies. We refer to the latter as 'servo-bump noise,' due to the common occurrence of noise peaks due to servo-loop feedback circuitry.

We have specifically considered the weak-noise regime, which is typical of modern qubit experiments. In this limit, we uncover simple relations between the underlying phase-noise spectra and noise spectra measured in self-heterodyne experiments. These relations are given in Eqs. (14), (28), and (29), and they allow us to analyze and fit experimental self-heterodyne data using specific white and servo-bump noise models, as described in Sec. III.

The weak-noise limit also allows us to solve a master equation, describing the effects of laser phase noise on Rabi oscillations, which we then use to calculate gate fidelities. We perform realistic numerical simulations of Rabi gates by generating random time series that include white and servo-bump phase noise. The results are well explained by our master equation solutions, yielding a deeper understanding of the decoherence process. Our main results are given in Eqs. (32), (79), (92), and (93).

In the case of servo-bump phase noise, we observe that gate errors are most prominent when the central frequency of the noise peak occurs near the Rabi frequency, as expected for $T_{1\rho}$-type noise mechanisms [4]. We find the gate-error peak frequency falls in the range $1 \leq f_g/(\tilde{\Omega}_0/2\pi) < 1.5$, for which the worst-case gate error is given by Eq. (80). Away from this peak, the gate error due may be suppressed by many orders of magnitude, such that the residual errors are dominated by background noise (e.g., weak white noise). Generally, the contributions to the gate error from different noise mechanisms are found to be additive in the weak-noise regime.

To demonstrate how these results may be used to guide future qubit experiments, we consider the case of π-rotations ($N = 1/2$), in two-photon gates. If a servo bump is present and its peak frequency occurs near the Rabi frequency of one of the two transitions, then achieving a gate-error level of 10^{-3} would require a total (integrated) servo bump noise power of no more than $s_g = 0.0016$. (Note that s_g, as defined here, includes the power in the servo bumps on both sides of the carrier peak.) Similarly, a gate-error level of 10^{-4} would require a servo bump power of no more than $s_g = 0.00016$. In the self-heterodyne noise measurements analyzed in Sec. III, we observe a noise power of $s_g = 0.00027$ in one of the servo bumps, and $s_g = 0.00013$ in the other. Moreover, since the peak frequency of the larger servo bump occurs

at $f_g = 234$ kHz, we can suppress its effect on the fidelity by choosing a Rabi frequency of $\sim 117\times 2\pi$ kHz, or alternatively, a Rabi frequency larger than 1 or $2\times 2\pi$ MHz. In this way, we can realistically expect to achieve gate errors below 10^{-4} in this system.

[1] E. Geva, R. Kosloff, and J. L. Skinner, "On the relaxation of a two-level system driven by a strong electromagnetic field," J. Chem. Phys. **102**, 8541 (1995).

[2] Yu. Makhlin and A. Shnirman, "Dephasing of qubits by transverse low-frequency noise," JETP Lett. **8**, 497 (2003).

[3] G. Ithier, E. Collin, P. Joyez, P. J. Meeson, D. Vion, D. Esteve, F. Chiarello, A. Shnirman, Y. Makhlin, J. Schriefl, and G. Schön, "Decoherence in a superconducting quantum bit circuit," Phys. Rev. B **72**, 134519 (2005).

[4] F. Yan, S. Gustavsson, J. Bylander, X. Jin, F. Yoshihara, D. G. Cory, Y. Nakamura, T. P. Orlando, and W. D. Oliver, "Rotating-frame relaxation as a noise spectrum analyser of a superconducting qubit undergoing driven evolution," Nat. Commun. **4**, 2337 (2013).

[5] E. Paladino, Y. M. Galperin, G. Falci, and B. L. Altshuler, "$1/f$ noise: Implications for solid-state quantum information," Rev. Mod. Phys. **86**, 361 (2014).

[6] F. Yoshihara, Y. Nakamura, F. Yan, S. Gustavsson, J. Bylander, W. D. Oliver, and J.-S. Tsai, "Flux qubit noise spectroscopy using Rabi oscillations under strong driving conditions," Phys. Rev. B **89**, 020503 (2014).

[7] J. Jing, P. Huang, and X. Hu, "Decoherence of an electrically driven spin qubit," Phys. Rev. A **90**, 022118 (2014).

[8] S. de Léséleuc, D. Barredo, V. Lienhard, A. Browaeys, and T. Lahaye, "Analysis of imperfections in the coherent optical excitation of single atoms to Rydberg states," Phys. Rev. A **97**, 053803 (2018).

[9] M. Zhang, Y. Xie, J. Zhang, W. Wang, C. Wu, T. Chen, W. Wu, and P. Chen, "Estimation of the laser frequency noise spectrum by continuous dynamical decoupling," Phys. Rev. Appl. **15**, 014033 (2021).

[10] M. L. Day, P. J. Low, B. White, R. Islam, and C. Senko, "Limits on atomic qubit control from laser noise," npj Qu. Inf. **8**, 72 (2022).

[11] T. Okoshi, K. Kikuchi, and A. Nakayama, "Novel method for high resolution measurement of laser output spectrum," El. Lett. **16**, 630 (1980).

[12] G. Di Domenico, S. Schilt, and P. Thomann, "Simple approach to the relation between laser frequency noise and laser line shape," Appl. Opt. **49**, 4801 (2010).

[13] D. S. Elliott, R. Roy, and S. J. Smith, "Extracavity laser band-shape and bandwidth modification," Phys. Rev. A **26**, 12 (1982).

[14] M. Zhu and J. L. Hall, "Stabilization of optical phase/frequency of a laser system: application to a commercial dye laser with an external stabilizer," J. Opt. Soc. Am. B **10**, 802 (1993).

[15] Sine and cosine integral functions are defined as $\mathrm{Si}(z) = \int_0^z (\sin t)/t\, dt$ and $\mathrm{Ci}(z) = -\int_z^\infty (\cos t)/t\, dt$.

[16] Phys. Rev. Lett..